Rigidity Preserving Image Transformations and Equivariance in Perspective

Lucas Brynte*, Georg Bökman*, Axel Flinth, Fredrik Kahl

Department of Electrical Engineering, Chalmers University of Technology, Gothenburg, Sweden

February 1, 2022

Abstract

We characterize the class of image plane transformations which realize rigid camera motions and call these transformations 'rigidity preserving'. In particular, 2D translations of pinhole images are not rigidity preserving. Hence, when using CNNs for 3D inference tasks, it can be beneficial to modify the inductive bias from equivariance towards translations to equivariance towards rigidity preserving transformations. We investigate how equivariance with respect to rigidity preserving transformations can be approximated in CNNs, and test our ideas on both 6D object pose estimation and visual localization. Experimentally, we improve on several competitive baselines.

Keywords: Equivariance, 3D computer vision

1 Introduction

An important property of convolution operators (e.g., linear convolutional layers in neural networks) is their translation equivariance, i.e. that translation and application of the network commutes. Put in slightly formal terms, we say that an operator Ψ is translationally equivariant if for each input f and each translation t, we have

$$\Psi(\Lambda_t f) = \Lambda_t(\Psi f),$$

where $\Lambda_t f(x) = f(x-t)$. Through a global average pooling, this equivariance can easily be turned in to an *invariance* as well, i.e. $\widehat{\Psi}(f) = \widehat{\Psi}(\Lambda_t f)$. It is clear that such properties might be beneficial when designing neural networks. To be concrete, consider a network designed for detecting the presence of a cat in an image. That network should react similarly to a cat in the lower right corner as to one the upper right corner – it should be invariant to translations. If the network instead should detect the position of the cat, the prediction should translate with the cat – this is equivariance.



Figure 1: Two pictures taken by the same camera, but with camera positions translated relative to each other. Notably, the depictions of an object in the two images are *not* translations of each other.

However, as we show in this paper, a translation of the camera does not correspond to translation of the image for any non-planar surface patch in the scene. See Figure 1 for an example. In fact, we can even prove that translations of the image do not correspond to images taken following any rigid camera movements. Since we, given a fixed camera, only can alter the image by performing such, we argue that one should consider a different set of image transformations, which do correspond to rigid movements of the camera. In the following, we will refer to such transformations as rigidity preserving image transformations (a precise definition is given in Section 2).

1.1 Related work

Convolutional layers have been the workhorse of neural networks for several decades [25, 34, 37]. Even though convolution operators yield translation equivariance, the whole network is typically not equivariant due to sub-

^{*}These authors contributed equally to this work

sampling and padding operations [33, 30]. Attempts to redesign modern CNNs to achieve translation equivariance have resulted in improved robustness, but degraded performance [1, 59]. In this paper, further evidence that translation equivariance may not be the ideal objective for perspective images is provided.

Our work is also related to spherical image representations, which are frequently used for wide-angle cameras, e.g., fish-eye cameras [43]. Recently, several frameworks for obtaining SO(3)-equivariance have been developed [13, 15, 19, 22, 23, 31]. However, ordinary perspective images, which can be mapped to the sphere, typically have a well-defined orientation, so SO(3)-equivariance is not necessarily desired. Mapping a perspective image to the sphere also yields a signal only on a small part of the sphere, which may severely limit performance for methods designed for signals on the entire sphere. A further complicating factor is that many of these approaches work in the spherical Fourier domain. We will work in the spatial domain and use some of the invariant properties of the sphere representation. From this viewpoint, our approach resembles methods that adapt standard CNNs to be applicable to spherical images [16, 21, 52], though this is not our aim.

Our pitch-yaw-group equivariant network construction is related to so called group convolutional neural networks [14, 36, 57]. In our setting, the approach boils down to applying a convolution kernel in a coordinate system defined by the azimuthal equidistant map projection. Another work drawing inspiration from map projections to define sampling schemes on the sphere is [20]. More information in general on map projections can be found in [50].

Data augmentation is a standard technique for increasing the amount of image data with slightly modified images. Various geometric transformations are used in the literature. For instance, in [49] cropping provides randomly translated image patches, in [10] scalings and rotations in the image plane are applied, and in [38] 2D affine transformations. More elaborate transformations, such as Möbius transformations [61] have also been investigated with improved performance and generalization as a result. More specifically, 2D homography augmentations are used in [55] for object detection. An augmented image is obtained by transforming the corners of the original image to four random points. In contrast to our approach, this procedure does not necessarily result in a possible image taken by the original camera. Systematic approaches for evaluating various data augmentation techniques can be found in, e.g., [17, 18, 60].

For neural networks that estimate 3D properties from images, e.g., 6D object pose estimation [10, 29, 41] and visual localization [8, 38, 46], data augmentation is a delicate matter since while the input image is transformed, the 3D target also has to undergo a corresponding transformation. As an example, in 6D object pose estimation,

an image rotation around the principal point corresponds to a 3D rotation around the optical axis of the object pose, cf. [10].

In [42], the object pose of objects in the images are rotated, and the resulting transformation of the image is approximated with a homography. This approach does not necessarily result in an image that could have been taken by the original camera. The type of augmentations we are considering in this article appears to only have been used in [12], which is the currently SOTA method for the LINEMOD dataset. In this article, we consolidate this approach by our theoretical considerations.

In [56], different geometric augmentation strategies are experimentally evaluated for pose estimation and it is found that some transformations (scaling and 2D translation) do not correspond to any camera motion and may degrade performance, while 2D rotation around the principal point is geometrically sound, and enhances performance in their experiments. This is consistent with our theoretical findings - the group of rigidity preserving image transformations is a subset of the homographies, which includes 2D rotation as a special case.

1.2 Paper content

Let us return to detecting the positions of cats in images. In the light of the translation equivariance property of CNN:s, one may ask the question whether there is any camera movement which results in an image translation? Intuitively, translating the camera is a candidate to consider. However, as can be seen in Figure 1, translating a pinhole camera does not result in a translation of the image. In fact, we will show that there is no rigid transformation of the camera resulting in an image translation, and furthermore characterize the image transformations that correspond to rigid camera rotations.

Contributions. In this paper, we develop a mathematical framework resting on the above observation. We show that if the depth of the depicted object is unknown, the rigidity preserving image transformations are given by a subset of the homography group which we call the rotational homographies (defined by having a matrix representation $H \in SO(3)$). In particular, there is no image translation that is precisely corresponding to camera translations.

We study different ways of ensuring equivariance with respect to rigidity preserving image transformations: either via design of the neural network architecture, or via data augmentation. In the former case, we introduce and analyze a new group structure on a subset of the homographies, coined the pitch-yaw-group, which exclude rotations in the image plane (which may be unwanted in some settings).

In the final part of the paper, we show that our ideas can be used to boost the performance of (i) the Efficient-Pose model [10] for 6D object pose estimation and (ii) the DSAC* Tiny model [8] for visual localization. In the appendix, we present a further experiment for visual localization using the Pixloc model [46].

Limitations. Although the aim of our work is to boost the performance of computer vision systems, we cannot expect this boost to be huge. After all, as can be seen in Figure 1, the effect of a rigid transformation of the camera compared to an image translation is subtle. Another limitation is that the camera intrinsics must be known.

The pitch-yaw group (defined in Section 3.1) can be applied to spherical images, but should not be seen as a new way of designing equivariant networks on the full sphere, since it creates large distortions far away from the north pole.

2 Rigidity preserving image transformations

We assume images acquired with a pinhole camera with known intrinsic calibration. Without loss of generality, we choose an orthonormal coordinate system (e_0, e_1, e_2) in \mathbb{R}^3 with the camera center at the origin, the optical axis along the x_2 -axis, and the image plane at $x_2 = 1$, so that a non-occluded 3D point at position $x = [x_0, x_1, x_2]^T \in \mathbb{R}^3$ with $x_2 > 0$ projects to an image point at position

$$\pi(x) = [x_0/x_2, x_1/x_2]^T \in \mathbb{R}^2.$$

To simplify notation, we may think of this as a point in the *projective plane* \mathbb{P}^2 , so that $\pi(x) = \begin{bmatrix} x_0, x_1, x_2 \end{bmatrix}^T$ in homogeneous coordinates. We model images as functions on \mathbb{P}^2 .

Let us now consider that an image is acquired by taking a picture of a scene consisting of a set of surfaces. For simplicity, we will assume that the scene consists of a regular surface $S \subset \mathbb{R}^3$. Importantly, we assume that the 3D shape and depth of the surface is unknown to us, and we only have access to its projection $\pi(S)$. If we move the surface (or by duality, the camera) using a rigid transformation, the pixels in the image representing the surface will also be transformed via some map. Let us name such transformations.

Definition 2.1. A rigidity preserving image transformation is a mapping $\eta: \mathbb{P}^2 \to \mathbb{P}^2$ for which there exists a regular surface S with unknown shape, and a rigid transformation ρ of \mathbb{R}^3 so that

$$\eta \circ \pi(x) = \pi \circ \rho(x), \text{ for all } x \in \mathbb{R}_{>0}S, \tag{1}$$

where $\mathbb{R}_{>0}S$ denotes the set of all positive multiples of elements in S, i.e. $\{\lambda x \mid \lambda > 0, x \in S\}$.

Remark 2.2. The unknown depth assumption is manifested in requiring (1) to hold for $x \in \mathbb{R}_{>0}S$, and not only S. Note that if depth information is available, one can always construct η by rendering S at two different camera locations (provided no occlusions occur).

A mapping $\mathbb{P}^2 \to \mathbb{P}^2$ is called a **homography** if it can be expressed as $x \mapsto y = Hx$ where H is a non-singular 3×3 matrix and x, y are 3-vectors of homogeneous coordinates representing the points in \mathbb{P}^2 . It turns out that the rigidity preserving image transformations are a subset of the homographies, namely the *rotational homographies*.

Definition 2.3. A homography H is a rotational homography if the matrix representing it is an element of SO(3). We denote the set of rotational homographies by RH.

This sets us up for our main theorem.

Theorem 2.4. Rigidity preserving image transformations correspond exactly to the rotational homographies RH. More precisely:

- (i) If η is a rigidity preserving image transformation, the rigid transformation ρ in (1) must be a pure rotation, that is, $\rho(x) = Rx$ for some $R \in SO(3)$.
- (ii) Every $R \in SO(3)$ gives rise to a rigidity preserving image transformation η , where the rigid transformation ρ in (1) is given by $\rho(x) = Rx$.

Proof. (i) Let $\rho(x) = Rx + t$, with $R \in SO(3)$ and assume that $t \neq 0 \in \mathbb{R}^3$. We will show by contradiction that t must be zero. Pick a point $u \in S$ such that Ru and t are linearly independent. Now, let $\lambda \neq 1$. We have $\pi(u) = \pi(\lambda u)$ and hence $\eta(\pi(u)) = \eta(\pi(\lambda u))$ for our rigidity preserving image transformation η . This, together with (1), implies that $\pi(\rho(u)) = \pi(\rho(\lambda u))$, i.e. that $\rho(u)$ and $\rho(\lambda u)$ are collinear. However, their crossproduct is non-zero:

$$\rho(u) \times \rho(\lambda u) = (Ru + t) \times (\lambda Ru + t) = (1 - \lambda)(Ru) \times t,$$

which leads to a contradiction, and hence, we can conclude that t=0.

(ii) Define η by $\eta(y) = Ry$, where y is a 3-vector of homogeneous coordinates. η is well defined since for every $\lambda \neq 0$ we have $\eta(\lambda y) = \lambda \eta(y)$ so that every homogeneous representation of y is mapped to a homogeneous representation of $\eta(y)$. It is obvious that η satisfies (1) with $\rho(x) = Rx$.

Remark 2.5.

• A careful inspection of the proof shows that (1) only needs to hold for $x \in \{\lambda y \mid \lambda \in U, y \in S\}$ for some neighborhood U of 1. This relaxed assumption can be interpreted as not having exact depth information.

• A translation in the image plane by a vector $\tau = \begin{bmatrix} \tau_0 & \tau_1 \end{bmatrix}^T$ can be written as a homography H with $H = \begin{bmatrix} I_{2\times 2} & \tau \\ 0 & 1 \end{bmatrix}$. Note, however, that this never corresponds to a rigidity preserving image transformation as H is not an orthogonal matrix.

The above proof relies heavily on the assumption of unknown depth. How much more can be done when the depth is known? Are the translations rigidity preserving then? The following proposition shows that unless we are taking an image of a 3D plane parallel to the image plane, a rigid camera motion can only be equivalent to an image translation on singular sets.

Proposition 2.6. Let τ be a translation in the image plane not equal to the identity. Suppose that for some rigid motion ρ and some set $S \subseteq \mathbb{R}^3 \setminus \{0\}$, $\tau \circ \pi = \pi \circ \rho$. Then S is a union of a continuous curve $\gamma : \mathbb{R} \setminus M \to \mathbb{R}^3$ (where M is a set of at most three points), and a union of either

- a plane parallel to span (e_0, e_1) , and possibly one more line.
- between one and three lines.

The proof is quite technical, and can be found in Appendix E.1. Its main idea is that $\tau(\pi(x)) = \pi(\rho(x))$ is equivalent to the existence of a $\lambda \in \mathbb{R}$ with $\lambda Hx = \rho(x) := Rx + t$ where H is the matrix defined in Remark 2.5. Up to λ for which $(\lambda H - R)$ is singular, the solutions are hence given by $(\lambda H - R)^{-1}t$, $\lambda \in \mathbb{R}$ – this is the curve referenced in the proposition. The rest of the proof consists in analyzing when $(\lambda H - R)$ is singular.

Theorem 2.4 and Proposition 2.6 should convince the reader that translations are not the most natural transformations of pinhole camera images, and that the rotational homographies RH are more suited. We will explore two alternative approaches for handling equivariance with respect to rigidity preserving image transformations in the next two sections. The first one is to develop neural networks that are equivariant by design. The second approach is to learn equivariance by data augmentation.

3 Rotational homography equivariance

Theorem 2.4 suggests that the natural equivariance for neural networks acting on images is *not* the group of translations, but rather the rotational homography group. Accordingly we should try to design networks that are equivariant with respect to this action. The following proposition shows that a straightforward relation between RH and SO(3) gives us a simple way to do this.

Proposition 3.1. (i) The rotational homographies RH form a subgroup of the group of diffeomorphisms on \mathbb{P}^2 . The

subgroup is isomorphic to SO(3) equipped with matrix multiplication.

(ii) Let ψ be an SO(3)-equivariant network. Then

$$\phi: f \mapsto (\psi(f \circ \pi)) \circ \pi^{-1}$$

is an RH-equivariant network. Here, π^{-1} maps into the upper half sphere.

The proofs can be found in. Appendix E.2 The result gives a direct way to design an RH-equivariant network: we transform the input image f to the spherical image $f \circ \pi$. Applying the SO(3)-equivariant network ψ to $f \circ \pi$ is then exactly equivalent to applying the RH-equivariant network ϕ to f!

3.1 The pitch-yaw group

There is a caveat to using a network with invariance (or equivariance, respectively) equivariance with respect to the entirety of RH. The group RH namely includes rotations in the image plane – these correspond exactly to the $h \in \text{RH}$ associated to R around the x_2 -axis. This behavior can sometimes be problematic. A somewhat contrived, but still relevant example, is given by a self-driving car. Full RH-invariance would mean that it cannot distinguish between a speed limit of 90 km/h and one of 06 km/h!

Hence, it can be beneficial to design a network which is only equivariant with respect to rotations around axes in the plane $\operatorname{span}(e_0, e_1)$. However, we have the following fact.

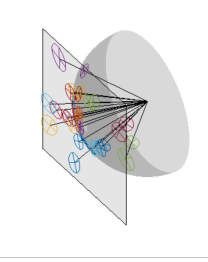
Proposition 3.2. No proper subgroup of SO(3) contains both the rotations around the x_0 -axis (pitches) and the rotations around the x_1 -axis (yaws).

The short proof using Euler angles can be found in Appendix E.3. Proposition 3.2 prohibits us from using any form of restriction of the action of SO(3) on the sphere to design a network only equivariant to pitches and yaws. To get an idea of what to do instead, let us notice that any rotation around an axis in the span(e_0, e_1)-plane can be written as $\exp(\alpha_0 C_0 + \alpha_1 C_1) \subseteq SO(3)$, where exp is the matrix exponential, and C_0 and C_1 are the skew-symmetric matrices corresponding to the linear maps $v \mapsto e_0 \times v$ and $v \mapsto e_1 \times v$, respectively. Such rotations will in the following be referred to as pitch-yaws. If we look at the "logarithms" $\alpha_0 C_0 + \alpha_1 C_1$ directly, we can define a group structure by addition on this set. We identify $\alpha_0 C_0 + \alpha_1 C_1$ with the vector $\alpha \in \mathbb{R}^2$.

Definition 3.3. We define PY as $span(C_0, C_1)$, and equip it with the group structure induced by vector addition.

Note that we cannot identify $\alpha \in PY$ with $\exp(\alpha) \in SO(3)$. The reason is that all $\tilde{\alpha}$ collinear with α and with $|\tilde{\alpha}| - |\alpha| \in 2\pi\mathbb{Z}$ correspond to the same element in SO(3). Thus, in this formulation, we would need to





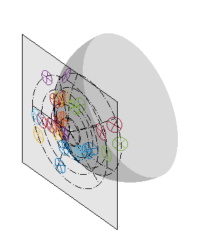




Figure 2: The two image representations. The pinhole camera model and the conventional image representation on \mathbb{P}^2 to the left, and our proposed pitch-yaw model and image on PY to the right, corresponding to the azimuthal equidistant map projection.

understand α as an equivalence class of collinear vectors. Since adding such equivalence classes does not necessarily result in a set of collinear vectors, our group would not be well-defined.

Given two functions F and G on PY, we may now define the group-convolution between them via

$$F * G(\alpha) = \int_{PY} F(\alpha - \beta)G(\beta)d\beta, \quad \alpha \in PY.$$
 (2)

Using such filter convolutions as linear layers in a network induces PY-equivariance.

Our spherical images are functions on the sphere, and not on PY. Given a function \hat{f} supported on $\mathbb{S}^2 \setminus \{-e_2\}$, we may however associate it with a function F on $U_{\pi} = \{\alpha \in \text{PY} \mid |\alpha| < \pi\}$ through $F(\alpha) = \hat{f}(\exp(\alpha)e_2)$, and trivially extend F with zero to define it on the whole of PY. In this way, we may convolve spherical images with filters on PY. Practically, this means that sampling the image in points $\{\exp(\alpha)e_2 \mid \alpha \in U_{\pi}\}$, where $G \subseteq \text{PY}$ is a regular grid, and applying a standard CNN to the resampled image, we obtain a network which is PY-equivariant.

This resampling is, up to a shift of the polar angle, to the azimuthal equidistant map projection [50]. This projection maps a point with spherical coordinates (ϑ, φ) on the sphere to the point with radius ϑ and polar angle φ in the plane. Similarly, we may characterize the mapping of an image on \mathbb{P}^2 to an image on PY as a simple radial transformation. More information is provided in Appendix E.4.

The azimuthal equidistant map projection is just one of many that can be used for mapping the sphere to a plane. Hence, there are many more strategies of resampling a spherical image and convolution (see for instance [4, 20, 16]). We leave it for future work to analyze other resampling strategies.

Remark 3.4. This construction may also be interpreted as a way to define an action $\chi_{\alpha}(\theta)$ of PY on the sphere (up to a set of measure zero), which in turn can be used to define the convolution with a filter on PY directly. For formal reasons, this action however really needs to be

defined on a countable union of distinct spheres instead, i.e. $\mathbb{N} \times \mathbb{S}^2$. We carry out the details in Appendix C.

3.2 The approximating property of PY

In Figure 2, we show an example of a spherical image being represented on \mathbb{P}^2 and on PY. The identical small spherical caps are clearly distorted by the projections onto \mathbb{P}^2 and PY, respectively. These distortions are however apparently less severe for the PY-representation.

We can analyze this via comparing the actions of PY and the corresponding elements in $\exp(PY)$, i.e. comparing PY-translating θ with α to rotating θ by the element $\exp(\alpha) \in SO(3)$. If the magnitude of α is small, and θ is close to the north pole e_2 , the two actions are very similar. Note that while this is not enough when full spherical images are concerned, it is acceptable in our setting: Unless using very wide lenses, images will be supported close to the principal point.

In Figure 3, we compare the distortions from using a PY-translation and a translation in the image plane, respectively, to approximate the action of applying the rotational homography associated with a pitch-yaw $\exp(\alpha)$. The transformations are chosen so that the origin is transformed to the same point as the rotation would do. As can be seen, the PY-group approximates the rotational homography significantly more faithfully than the translation. In Appendix D we analyze this further, and in particular bring formal mathematical results.

4 Rotational homography augmentation

By applying rigidity preserving image transformations, one can generate augmented images and corresponding camera poses, to be incorporated when training a neural network. In previous derivations, we assumed a special 3D coordinate system (cf. Section 2), which is not valid in practice. Therefore, we will describe the augmentation procedure in a general setting.







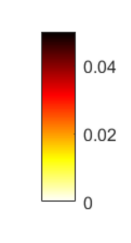


Figure 3: An image (in \mathbb{P}^2 -domain) to which a rotational homography (left) and the corresponding PY-translation (center) and conventional translation (right) has been applied. The overlay depicts the distortions compared to applying the rotational homography, measured in Euclidean distance of points on the sphere.

For a given camera with intrinsic calibration, represented by a 3×3 upper triangular matrix K, camera pose $R \in SO(3)$ and camera $c \in \mathbb{R}^3$, a point $x \in \mathbb{R}^3$ is projected to $y \in \mathbb{P}^2$ according to $\lambda y = KR \begin{bmatrix} I_3 & -c \end{bmatrix} \begin{bmatrix} x \\ 1 \end{bmatrix}$, where λ is a scaling factor and I_3 is the identity matrix, see [26]. If we warp the original image f with the homography $H = KR_{\text{aug}}K^{-1}$, we will get a new image f_{aug} , where the image coordinates are related by $y_{\text{aug}} = Hy$. Then, the pose for the augmented camera should be $R_{\text{aug}}R$ with unchanged position at c, which can be verified by checking that the camera equation still holds:

$$\lambda y' = \lambda H y = HKR \begin{bmatrix} I - c \end{bmatrix} \begin{bmatrix} x \\ 1 \end{bmatrix} = KR_{\text{aug}}R \begin{bmatrix} I - c \end{bmatrix} \begin{bmatrix} x \\ 1 \end{bmatrix}.$$

Remark 4.1. In many computer vision applications, there may be several cameras with different intrinsic calibrations involved. In such cases, it makes sense to augment with the homography $H = K'R_{\text{aug}}K^{-1}$ where K' is another calibration matrix. This is equivalent to performing augmentation with a general homography as any 3×3 matrix homography H can be written in this form.

5 Experiments

To demonstrate the effectiveness of our proposed sampling scheme and data augmentation, we carry out experiments on 6D object pose estimation and visual localization. The code used in the experiments is provided as a supplement.

5.1 6D object pose estimation

Datasets. Experiments are carried out on LINEMOD as well as Occlusion LINEMOD. LINEMOD is a standard benchmark for 6D object pose estimation [28]. The dataset consists of 15 RGB-D indoor image sequences where objects are laid out on a table with cluttered background. For each sequence there is a corresponding object of interest put at the center, for which a CAD model is available. We disregard two of the objects with low

quality CAD models, and disregard the depth channel as input, as is the case for [10] and many works before them. The Occlusion LINEMOD dataset was produced by [5] by taking one of the LINEMOD sequences and annotating the pose of the surrounding 8 objects. These often partially occluded objects make up the objects of interest for this dataset. For experiments on LINEMOD, we conventionally split each sequence into training and test data as e.g. [10, 45, 7], with ~ 200 samples for training and ~ 1000 samples for test. For Occlusion LINEMOD, the very same approach is taken. Note however that while consistent with [10], with which we compare our results, this is not consistent with all other works performing experiments on Occlusion LINEMOD. As is conventional, we use the ADD(-s)-0.1D metric [28] to evaluate our experiments.

Models. We compare with the EfficientPose [10] method as a baseline. This model is the second best performing model on the LINEMOD dataset, only surpassed by [12]. However, since the latter have not released their code at the time of writing this article, we have unfortunately not been able to perform similar experiments on that model.

The size of the EfficientPose model is governed by a single hyperparameter ϕ . Experiments are performed in two settings: (1) pitch-yaw equivariance (PY), and (2) rotational homography data augmentation (RH_{aug}). For the PY-equivariance setting, rather than applying the CNN of EfficientPose directly on our observed images, the images are first warped to the PY domain. While EfficientPose, and many others, apply geometric data augmentation in the form of image rescale and image rotation, in our second setting we also apply a subsequent pitch-yaw rotational homography during augmentation. For further details, see Appendix B.1.

Training was done in accordance with [10], apart from a few adjustments. To speed up training, we used a larger batch-size and adjusted learning rate for the $\phi=0$ -model. We made two larger modifications to the code base: (1) enabling reshuffling at every epoch start (2) refraining from cherry-picking the optimal model over all epochs, w.r.t. the ADD(-s)-0.1D metric on the test set.

Experiment setting	$\phi = 0$		$\phi = 3$		
Experiment setting	Roll 180°	Roll 45°	Roll 180°	Roll 45°	
Baseline	77.44% (79.04%)	76.98%	81.94% (83.98%)	78.92%	
PY	80.47%	81.03%	82.91%	82.76%	
$ m RH_{aug}$	81.92%	83.58%	85.20%	84.92%	

Table 1: Object pose results on Occlusion LINEMOD. The reported results are median results over three runs. Results reported by [10] in parenthesis.

EP: Baseline	EP: PY	EP: RH _{aug}	DPOD^{+1}	$PVNet^2$	HybridPose ³	$CDPN^4$	BPnP^5	DFPN-6D ⁶
95.56% (97.35%)	97.09%	97.21%	95.15%	86.27%	94.5%	89.86%	93.27%	98.06%
$^{1}[58], ^{2}[45], ^{3}[51], ^{4}[39], ^{5}[11], ^{6}[12].$								

Table 2: Comparison of 6D object pose results. The EP results (ours) are medians of three runs. Results reported by [10] in parentheses.

For all baseline experiments, models are retrained with these proper modifications, enabling a fair comparison. For further details, see Appendix B.1.

In all experiments, data augmentation is performed as follows. First, image rescaling is applied with a factor sampled uniformly from [0.7, 1.3]. Furthermore, image plane rotations are carried out around the principal point, with a 'roll' angle uniformly sampled from [-180, 180] by default. This is all consistent with [10]. Further, we experiment with more realistic reduced 'roll' angles sampled from [-45, 45]. Finally, in the RH_{aug} case, a random homography is applied corresponding to a camera pitch-yaw rotation with an angle sampled uniformly from [-20, 20].

Results. In Table 1, results on Occlusion LINEMOD are presented. Each reported result is the median score of three training runs. As expected, there is some discrepancy between the baseline trained by us and the original reported results, in particular due to not cherry-picking the best performing epoch (see above). The models trained with PY-images perform consistently better than the baseline and the RH-augmented models perform even better. That augmentation is beneficial is not surprising, considering that the dataset only has ~ 180 training images.

For all further experiments, we used the smaller $\phi=0$ model, as it is much more feasible to train. We also choose to moderate the 'roll' augmentations to a maximum of 45° when combined with RH_{aug}, since this proved superior for the limited capacity $\phi=0$ model on Occlusion LINEMOD.

In Table 2, results on LINEMOD with the ADD(-S)-0.1D metric are presented, along with a comparison to other methods. From these results, we see that incorporating either our rotational homography augmentation $\rm RH_{aug}$ or the PY-equivariance, the median performance of EfficientPose is increased. We do not quite reach the SOTA performance reported in [12] – note however that that method already applies a form of RH-augmentation.

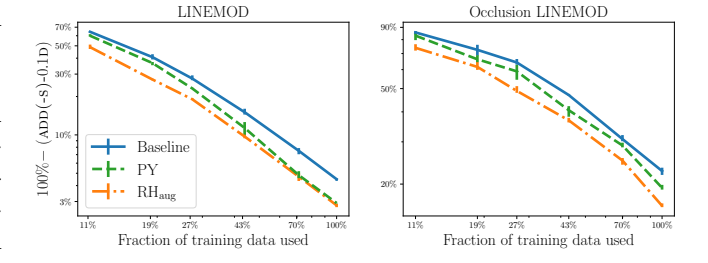


Figure 4: Left: Results of the limited data experiments for the LINEMOD dataset. Right: Results of the limited data experiments for the Occlusion LINEMOD dataset. In both log-log plots, the line follows the median of three trials, whereas the error bars indicate the best and worst of the trials.

Limited data. To further investigate the role of equivariance, we perform a small ablation study by artificially limiting the data. For each sequence in the LINEMOD dataset, as well as the Occlusion LINEMOD dataset, we create five new training sets by randomly choosing a subset of $n \in \{20, 35, 50, 80, 130\}$ images to train on, respectively (the total number is between 173 and 189 depending on the sequence). Each experiment is repeated three times, to mitigate the issue of statistical fluctuations. Apart from that, we use the same hyperparameters as in the previous experiments. In Figure 4, we plot the error (i.e. 100% - (ADD(-s)-0.1D)) against the amount of training data, averaged over the sequences. We see that for all fractions of data on both datasets, data augmentations consistently performs best, which is not surprising in the limited data context. It is equally clear that the PY-equivariant nets also consistently outperforms the baseline nets.

For the LINEMOD-experiments in particular, we note a special effect of the equivariance. Due to the doubly logarithmic scales, the figure suggests that the error drops at a power law rate with increasing amount of data for all models. However, the rate is clearly higher for the PY-equivariant nets compared to the other. Let

Experiment	PY+GeomAug	Baseline+GeomAug	$\mathrm{RH}_{\mathrm{aug}}$	Baseline	PY
Pose within 5cm/5°	71.6 %	69.5%	68.0%	65.5%	64.9%

Table 3: Results on 7-Scenes. The scores are the proportion of test images with pose error within 5cm and 5°.

us note that a similar effect of introducing equivariance in a neural network was noticed in [3] in a completely different context using an entirely different network (calculation of interatomic potentials, which are invariant to rotations of the molecules). This further suggests that PY-equivariance helps the model to generalize, and thus seems to be the 'correct' equivariance to strive for. See also [27] for a discussion about the appearance of a power law relation between amount of data and error for various deep learning models.

This effect is not as prominent for the Occlusion LINEMOD dataset - we speculate that the dataset is too small for this more delicate learning task for the model to enter the region where the the equivariance effect kicks in. Note that in the LINEMOD plot, the PY-model error only falls steeper in the region wich much data.

In Appendix F further results are presented, including per-object results. Furthermore, empirical evidence is given for the choice of representation for the rotation regression targets in the PY setting, as described in Appendix B.1.

5.2 Visual localization

In this section we present experiments using DSAC* Tiny on the 7-Scenes dataset.

Dataset. We perform visual localization experiments on the 7-Scenes dataset [48] consisting of collections of images of 7 different scenes, taken by a Kinect camera. We discard the depth information and estimate the camera pose from a single RGB image.

Model. Our experiments build on DSAC* Tiny [8] and the code available at [9]. DSAC* is an end-to-end learning method. In RGB-mode, it uses a CNN to predict dense 2D-3D correspondences which are then used to estimate the camera pose using differentiable RANSAC [6]. For more details we refer the reader to [8] and Appendix B.2, where we also explain modifications we made to the code. DSAC* Tiny is a small version of DSAC*, requiring only 4MB of memory. We work with a small model as we expect that equivariance will matter more when the model has low representational power.

We test five different training setups: Baseline (no augmentation except color jitter), PY (resampling the image to the PY-domain, still only with color jitter augmentation) Baseline+GeomAug, PY+GeomAug, (as the Baseline and PY models, but additionally augmenting with image size changes and small rotations in the image

plane) and $\mathrm{RH}_{\mathrm{aug}}$ (Baseline augmented with both Geomaug and homographies in RH). Implementation details for the resampling and data augmentation are presented in Appendix B.2.

Results. The accuracy averaged over the test images in all scenes is presented in Table 3. More detailed results for the individual scenes can be found in Appendix F. Each reported result is from a single run of training (per scene). It is clear from Table 3 that data augmentation gives a performance boost. The best performance is obtained by PY+GeomAug, which we speculate is a good trade-off between homogenizing the data by resampling it and still having diverse realistic training examples provided by the augmentation. Correspondingly, the performance of RH_{aug} is slightly worse compared to Baseline+GeomAug. This might be due to the low capacity of the DSAC* Tiny model, as the diversity of the training set is increased substantially with the added augmentations.

Additional experiments. In Appendix A, we present experiments for visual localization using another model, Pixloc [46]. The results are less conclusive than the ones presented here, but still to some extent further support the hypothesis that PY-equivariance is beneficial.

6 Conclusions

We present a framework for handling perspective effects in images taken by a pinhole camera. More specifically, we provide a mathematical argument for why translation equivariance is not the ideal objective and that it is more natural to either design networks that are equivariant to camera rotations simulate camera rotations when performing data augmentation. As an alternative to true equivariance with respect to camera rotation, we also present and analyse a group structure (PY) on the set of rotations around axes in the image plane. Our framework is generally applicable and can easily be integrated into existing CNN architectures. We have tested our framework on two different applications that rely on CNNs for estimating 3D pose, and report promising results indicating that increased rotation equivariance can be beneficial.

Acknowledgement: The authors acknowledge support from Chalmers AI Research (CHAIR). This work was partially supported by the Wallenberg AI, Autonomous Systems and Software Program (WASP) funded by the

Knut and Alice Wallenberg Foundation. The computations were enabled by resources provided by the Swedish National Infrastructure for Computing (SNIC) at Chalmers Centre for Computational Science and Engineering (C3SE) partially funded by the Swedish Research Council through grant agreement no. 2018-05973. The authors also wish to thank Kunal Chelani for technical support with the evaluation of the visual localization experiments on the CMU Extended Seasons dataset.

References

- [1] A. Azulay and Y. Weiss. Why do deep convolutional networks generalize so poorly to small image transformations? *Journal of Machine Learning Research*, 20(184):1–25, 2019.
- [2] H. Badino, D. Huber, and T. Kanade. Visual topometric localization. In 2011 IEEE Intelligent Vehicles Symposium (IV), pages 794–799, 2011.
- [3] S. Batzner, A. Musaelian, L. Sun, M. Geiger, J. P. Mailoa, M. Kornbluth, N. Molinari, T. E. Smidt, and B. Kozinsky. SE(3)-equivariant graph neural networks for data-efficient and accurate interatomic potentials. arXiv preprint arXiv:2101.03164, 2021.
- [4] W. Boomsma and J. Frellsen. Spherical convolutions and their application in molecular modelling. In *Neural Information Processing Systems*, 2017.
- [5] E. Brachmann, A. Krull, F. Michel, S. Gumhold, J. Shotton, and C. Rother. Learning 6D object pose estimation using 3D object coordinates. In *European Conf. on Computer Vision*, 2014.
- [6] E. Brachmann, A. Krull, S. Nowozin, J. Shotton, F. Michel, S. Gumhold, and C. Rother. DSACdifferentiable RANSAC for camera localization. In Proceedings of the IEEE Conference on Computer Vision and Pattern Recognition, pages 6684–6692, 2017.
- [7] E. Brachmann, F. Michel, A. Krull, M. Y. Yang, S. Gumhold, and C. Rother. Uncertainty-driven 6D pose estimation of objects and scenes from a single rgb image. In *IEEE/CVF Conf. Computer Vision* and Pattern Recognition, 2016.
- [8] E. Brachmann and C. Rother. Visual camera relocalization from RGB and RGB-D images using DSAC. *TPAMI*, 2021.
- [9] E. Brachmann and Q. Yan. DSAC*. https://github.com/vislearn/dsacstar, 2020.
- [10] Y. Bukschat and M. Vetter. EfficientPose: An efficient, accurate and scalable end-to-end 6D multi object pose estimation approach. *Preprint* arXiv:2011.04307, 2020.

- [11] B. Chen, A. Parra, J. Cao, N. Li, and T.-J. Chin. End-to-end learnable geometric vision by backpropagating pnp optimization. In *IEEE/CVF Conf.* Computer Vision and Pattern Recognition, 2020.
- [12] J. Cheng, P. Liu, Q. Zhang, H. Ma, F. Wang, and J. Zhang. Real-time and efficient 6-d pose estimation from a single rgb image. *IEEE Transactions on Instrumentation and Measurement*, 70:1–14, 2021.
- [13] T. Cohen, M. Weiler, B. Kicanaoglu, and M. Welling. Gauge equivariant convolutional networks and the icosahedral CNN. In *Int. Conf. on Machine Learning*, 2019.
- [14] T. Cohen and M. Welling. Group equivariant convolutional networks. In *Int. Conf. on Machine Learning*, 2016.
- [15] T. S. Cohen, M. Geiger, J. Köhler, and M. Welling. Spherical CNNs. In *Int. Conf. on Learning Repre*sentations, 2018.
- [16] B. Coors, A. Paul Condurache, and A. Geiger. SphereNet: Learning spherical representations for detection and classification in omnidirectional images. In *European Conf. on Computer Vision*, 2018.
- [17] E. D. Cubuk, B. Zoph, D. Mane, V. Vasudevan, and Q. V. Le. AutoAugment: Learning augmentation policies from data. In *IEEE/CVF Conf. Computer* Vision and Pattern Recognition, 2019.
- [18] E. D. Cubuk, B. Zoph, J. Shlens, and Q. V. Le. RandAugment: Practical automated data augmentation with a reduced search space. In *Neural Information Processing Systems*, 2020.
- [19] M. Defferrard, M. Milani, F. Gusset, and N. Perraudin. DeepSphere: A graph-based spherical CNN. In Int. Conf. on Learning Representations, 2019.
- [20] M. Eder and J.-M. Frahm. Convolutions on spherical images. In IEEE/CVF Conference on Computer Vision and Pattern Recognition Workshops, 2019.
- [21] M. Eder, M. Shvets, J. Lim, and J.-M. Frahm. Tangent images for mitigating spherical distortion. In IEEE/CVF Conf. Computer Vision and Pattern Recognition, 2020.
- [22] C. Esteves, C. Allen-Blanchette, A. Makadia, and K. Daniilidis. Learning SO(3) equivariant representations with spherical CNNs. In *European Conf. on Computer Vision*, 2018.
- [23] C. Esteves, A. Makadia, and K. Daniilidis. Spinweighted spherical CNNs. In *Neural Information Processing Systems*, 2020.

- [24] M. A. Fischler and R. C. Bolles. Random sample consensus: a paradigm for model fitting with application to image analysis and automated cartography. Commun. Assoc. Comp. Mach., 24:381–395, 1981.
- [25] K. Fukushima. Neocognitron: A self-organizing neural network model for a mechanism of pattern recognition unaffected by shift in position. *Biol. Cybernetics*, 36:193—202, 1980.
- [26] R. I. Hartley and A. Zisserman. Multiple View Geometry in Computer Vision. Cambridge University Press, 2004. Second Edition.
- [27] J. Hestness, S. Narang, N. Ardalani, G. Diamos, H. Jun, H. Kianinejad, M. Patwary, M. Ali, Y. Yang, and Y. Zhou. Deep learning scaling is predictable, empirically. arXiv preprint arXiv:1712.00409, 2017.
- [28] S. Hinterstoisser, V. Lepetit, S. Ilic, S. Holzer, G. Bradski, K. Konolige, and N. Navab. Model based training, detection and pose estimation of texture-less 3D objects in heavily cluttered scenes. In Asian Conf. Computer Vision. Springer, 2013.
- [29] Y. Hu, P. Fua, W. Wang, and M. Salzmann. Single-stage 6D object pose estimation. In *IEEE/CVF Conf. Computer Vision and Pattern Recognition*, 2020.
- [30] M. A. Islam, S. Jia, and N. D. B. Bruce. How much position information do convolutional neural networks encode? In *International Conference on Learning Representations*, 2020.
- [31] C. Jiang, J. Huang, K. Kashinath, P. Marcus, M. Niessner, et al. Spherical CNNs on unstructured grids. In *Int. Conf. on Learning Representations*, 2019.
- [32] A. Jung et al. imgaug. https://github.com/aleju/imgaug, 2020.
- [33] O. S. Kayhan and J. C. v. Gemert. On translation invariance in cnns: Convolutional layers can exploit absolute spatial location. In *Proceedings of the IEEE/CVF Conference on Computer Vision and Pattern Recognition (CVPR)*, June 2020.
- [34] A. Krizhevsky, I. Sutskever, and G. E. Hinton. Imagenet classification with deep convolutional neural networks. In *Neural Information Processing Systems*, 2012.
- [35] A. Kundu, Y. Li, and J. M. Rehg. 3D-RCNN: Instance-Level 3D Object Reconstruction via Render-and-Compare. In 2018 IEEE/CVF Conference on Computer Vision and Pattern Recognition, pages 3559–3568, June 2018. ISSN: 2575-7075.

- [36] L. Lang and M. Weiler. A Wigner-Eckart theorem for group equivariant convolution kernels. In *Inter*national Conference on Learning Representations, 2020.
- [37] Y. LeCun, B. Boser, J. S. Denker, D. Henderson, R. E. Howard, W. Hubbard, and L. D. Jackel. Backpropagation applied to handwritten zip code recognition. *Neural Computation*, 1(4):541–551, 1989.
- [38] X. Li, S. Wang, Y. Zhao, J. Verbeek, and J. Kannala. Hierarchical scene coordinate classification and regression for visual localization. In *IEEE/CVF* Conf. Computer Vision and Pattern Recognition, 2020.
- [39] Z. Li, G. Wang, and X. Ji. CDPN: Coordinatesbased disentangled pose network for real-time RGBbased 6-DoF object pose estimation. In *IEEE/CVF* Int. Conf. on Computer Vision, 2019.
- [40] T.-Y. Lin, M. Maire, S. Belongie, J. Hays, P. Perona, D. Ramanan, P. Dollár, and C. L. Zitnick. Microsoft COCO: Common objects in context. In *European Conf. on Computer Vision*, 2014.
- [41] Y. Liu, Y. Yixuan, and M. Liu. Ground-aware monocular 3D object detection for autonomous driving. *IEEE Robotics and Automation Letters*, 6(2):919–926, 2021.
- [42] S. Mahendran, H. Ali, and R. Vidal. 3D Pose Regression Using Convolutional Neural Networks. In 2017 IEEE Conference on Computer Vision and Pattern Recognition Workshops (CVPRW), pages 494–495, July 2017. ISSN: 2160-7516.
- [43] H. Matsuki, L. von Stumberg, V. Usenko, J. Stückler, and D. Cremers. Omnidirectional DSO: Direct sparse odometry with fisheye cameras. *IEEE Robotics and Automation Letters*, 3(4):3693–3700, 2018.
- [44] I. Najfeld and T. Havel. Derivatives of the matrix exponential and their computation. *Advances in Applied Mathematics*, 16(3):321–375, 1995.
- [45] S. Peng, Y. Liu, Q. Huang, X. Zhou, and H. Bao. Pvnet: Pixel-wise voting network for 6dof pose estimation. In *IEEE/CVF Conf. Computer Vision and Pattern Recognition*, 2019.
- [46] P.-E. Sarlin, A. Unagar, M. Larsson, H. Germain, C. Toft, V. Larsson, M. Pollefeys, V. Lepetit, L. Hammarstrand, F. Kahl, and T. Sattler. Back to the Feature: Learning robust camera localization from pixels to pose. In CVPR, 2021.
- [47] P.-E. Sarlin, A. Unagar, M. Larsson, H. Germain, C. Toft, V. Larsson, M. Pollefeys, V. Lepetit,

- L. Hammarstrand, F. Kahl, and T. Sattler. Back to the Feature: Learning robust camera localization from pixels to pose. https://github.com/cvg/pixloc, commit 0072dc7, 2021.
- [48] J. Shotton, B. Glocker, C. Zach, S. Izadi, A. Criminisi, and A. Fitzgibbon. Scene coordinate regression forests for camera relocalization in RGB-D images. In *IEEE/CVF Conf. Computer Vision and Pattern Recognition*, 2013.
- [49] K. Simonyan and A. Zisserman. Very deep convolutional networks for large-scale image recognition. In *Int. Conf. on Learning Representations*, 2015.
- [50] J. P. Snyder. Map projections—A working manual, volume 1395. US Government Printing Office, 1987.
- [51] C. Song, J. Song, and Q. Huang. HybridPose: 6D object pose estimation under hybrid representations. In *IEEE/CVF Conf. Computer Vision and Pattern Recognition*, 2020.
- [52] Y.-C. Su and K. Grauman. Kernel transformer networks for compact spherical convolution. In IEEE/CVF Conf. Computer Vision and Pattern Recognition, 2019.
- [53] M. Tan, R. Pang, and Q. V. Le. EfficientDet: Scalable and efficient object detection. In IEEE/CVF Conf. Computer Vision and Pattern Recognition, 2020.
- [54] C. Toft, W. Maddern, A. Torii, L. Hammarstrand, E. Stenborg, D. Safari, M. Okutomi, M. Pollefeys, J. Sivic, T. Pajdla, F. Kahl, and T. Sattler. Longterm visual localization revisited. *IEEE Transac*tions on Pattern Analysis and Machine Intelligence, pages 1–1, 2020.
- [55] K. Wang, B. Fang, J. Qian, S. Yang, X. Zhou, and J. Zhou. Perspective Transformation Data Augmentation for Object Detection. *IEEE Access*, 8:4935– 4943, 2020.
- [56] Y. Wang. Data augmentation study for learningbased 6D pose estimation. Master's thesis, EPFL, Switzerland and Chalmers University of Technology, Sweden, 2021.
- [57] D. Yarotsky. Universal approximations of invariant maps by neural networks. Constructive Approximation, pages 1–68, 2021.
- [58] S. Zakharov, I. Shugurov, and S. Ilic. DPOD: 6D pose object detector and refiner. In *IEEE/CVF Int.* Conf. on Computer Vision, 2019.
- [59] R. Zhang. Making convolutional networks shiftinvariant again. In *ICML*, 2019.

- [60] X. Zhang, Q. Wang, J. Zhang, and Z. Zhong. Adversarial AutoAugment. In Int. Conf. on Machine Learning, 2020.
- [61] S. Zhou, J. Zhang, H. Jiang, T. Lundh, and A. Y. Ng. Data augmentation with Mobius transformations. *Mach. Learn.: Sci. Technol.*, 2(2):025016, 2021.

A Extra experiments

Here we present an extra visual localization experiment on the CMU Extended Seasons dataset. We again modify an existing model, Pixloc [46], using the methods developed in the main article.

A.1 Pixloc on CMU Seasons

Model. The idea of Pixloc is to use a U-net to learn feature maps and calculate them for query images. The same features are computed for reference images with known pose, the reference images are found by image retrieval. One then optimizes using Levenberg-Marquardt for the query pose giving the best match between the features of a 3D model projected into both the query and reference images. For details about the Pixloc model, we refer to [46]. Notably, we are using a revised version of the code made available by Sarlin et al. in the github repository [47] after the publication of the article.

Dataset. We use the CMU Extended Seasons dataset [2, 54]. This dataset is collected using car-mounted cameras, producing images with a significant amount of radial distortion. [46] take the radial distortion into account, e.g. when projecting the 3D models to the image plane, by considering a radial polynomial distortion model. Notably, this radial polynomial model is already quite close to our map between $\mathbb{P}^2 \to \mathrm{PY}$. However, they do not use their model to undistort the images before training. This means that the baseline model should perform similarly to the model trained on PY-warped versions of the undistorted images. To more clearly examine the effect of our methods, we therefore include a version of the model where perform the undistortion. See Figure 6 for an example of how similar the original and PY-warped images are in this case. Details on the implementation and data are given in B.3.

Similarly as in the LINEMOD experiment, we train the model on a randomly subsampled fraction of the original data. The fractions we consider are $(4^{-k})_{k=0,1,2,...,5}$. Here we subsample the query images but let the reference image set stay intact, in order to let the distance in pose from the query to the nearest reference be similar in the training and test sets.

Results. We use four models in our experiments: A model trained on PY-warped images, a model trained on undistorted images, a version with small RH-augmentations on undistorted images as well as a version with RH-augmentations on undistorted images that are afterwards warped to the PY-domain. The last experiment is dubbed RH_{aug}+PY. We measure the performance by the recall of the model at an error threshold of 25cm for the translation and 2° for the rotation. The results are presented in Figure 5. Similarly as in the LINEMOD experiments, we plot the error rate for the different methods, i.e. 100%— recall. The results do not give a conclusive answer to which setup performs the best across all data amounts and sequences. We can however see some trends.

First, there is a tendency for the two augmented methods to work better on the park dataset, and worse on the urban dataset, with the suburban dataset somewhere in the middle. That the success for data augmentation is dependent on the test sequence is plausible – if the sequence is more diverse, more data should be needed, whence data augmentations gives a more significant boost. The fact that the park set is the most difficult of the three further supports this argument. On the CMU Extended Seasons dataset the initial pose in Pixloc obtained from image retrieval is commonly quite close in rotation to the correct pose, because the images are often taken along straight roads. This also partially explains why data augmentation with altered rotations is not very successful for the urban and suburban data subsets.

Secondly, and more interestingly for us, we see that when we compare the PY-warped to the undistorted method, the warped methods consistently perform better for smaller data amounts: Out of the 9 possible comparisons up to fraction 4^{-3} of the data, the warped version is better each time. Interestingly, the same is true for the augmented methods: here, the model trained on augmented undistorted data performs worse than the model trained on warped data in 7 out of the 9 experiments for data fraction less than or equal to 4^{-3} . This to some extent supports the hypothesis that when data is scarce, the PY-equivariance of the warped model helps the network generalize.

The saturation of the results around data fraction 4^{-2} can potentially be explained by the huge amount of data. At this fraction there are around 12k query-ref image pairs available to the model, and they are each seen on average only around ten times during the duration of the training procedure. For details about the data fractions and training see Section B.3. We can speculate that in the lower data region before the saturation point, the errors again follow a power law distribution as discussed in Section 5.1 for the EfficientPose experiments, but more experiments would be needed to confirm this.

As was previously stated, we are building a model using an updated version of the Pixloc code. Therefore, we reran the updated code without any of our modifications to use as a baseline. Unfortunately, all such runs

Recall at (25cm, 2°)

1.0

66.4%

65.0%

64.8%

URBAN	Non-aug	gmented	RH _{aug} -ai	ugmented
UNDAN	Undist.	PY	Undist.	PY
Data fraction 4^{-5}	79.5%	80.5%	77.3%	79.8%
4^{-4}	85.5%	86.4%	84.3%	85.6%
4^{-3}	89.0%	89.6%	89.0%	88.9%
4^{-2}	90.3%	90.0%	89.2%	89.2%
4^{-1}	90.6%	90.3%	89.3%	89.0%
1.0	91.1%	90.5%	88.9%	88.9%
SUBURBAN	Non-aug			ugmented
	Undist.	PY	Undist.	PY
Data fraction 4^{-5}	69.6%	72.1%	69.0%	71.7%
4^{-4}	77.3%	78.3%	78.2%	79.9%
4^{-3}	82.0%	82.1%	82.6%	82.5%
4^{-2}	82.6%	83.3%	83.2%	82.7%
4^{-1}	83.1%	83.4%	82.4%	81.9%
1.0	83.5 %	82.9%	82.6%	82.7%
PARK	Non-aug			ugmented
	Undist.	PY	Undist.	PY
Data fraction 4^{-5}	49.9%	52.7 %	50.5%	51.7%
4^{-4}	58.9%	59.6%	60.8%	61.2 %
4^{-3}	63.1%	63.4%	64.2%	64.7 %
4^{-2}	63.9%	65.0%	66.2%	65.5%
4^{-1}	65.8 %	65.5%	64.8%	63.9%

Fraction of training query images used

6.3%

25.0%

100.0%

1.6%

0.4%

Figure 5: Results for the Pixloc experiments on the urban, suburban and park subsets of the CMU Extended Seasons test data presented in two different ways. Left: detailed presentation of the test recall (higher is better). Right: log-log plot of the recall error (lower is better).

65.3%



Figure 6: Example of the warping procedure on the CMU Extended Seasons data. Top: original image, middle: undistorted version, bottom: PY-warped version. This dataset is a special case among our experiments, where the original images are already heavily radially distorted and hence similar to the PY-warped versions.

except the one using the entire dataset and the one using a data fraction of 4^{-5} suffered from numerical problems and halted prematurely with NaN-values in the weights and losses, despite using the same hyperparameters as the other runs. We are unsure why this happened - we speculate that it might have to with differences in Pytorch or CUDA version from the authors and "unlucky" sampling of training batches, but ultimately, we do not have a satisfying explanation. Other users have reported similar issues to the github project. For the runs that did not halt prematurely, we got the following results: When training on the entire dataset, the baseline obtained a recall of 89.7%, 82.1% and 64.7% on the urban, suburban and park test sets, respectively, which is better than 88.3%, 79.6% and 61.0% for the old model (not the up-to-date code on github) trained on the entire dataset as reported in [46]. The run only using a fraction of 4^{-5} of the data instead obtained a recall of 80.8%, 70.7% and 51.7%, respectively. The baseline results are quite similar to the results obtained by the warped model, achieving 90.5%, 82.9%, 65.0% on the full data, and 80.5%, 72.1%, 52.7% for the low data amount. This is expected since, as mentioned earlier, the radial distortion present in the original images is quite close to our PY-model, which can be seen visually in Figure 6. We therefore expect that the similarity between the PY-runs and baseline would be high for all other data amounts as well had the baseline runs not experienced numerical issues and halted.

B Implementation details

B.1 EfficientPose

B.1.1 Pitch-yaw equivariance

Here, we describe in detail how modify the images to achieve a PY-equivariant architechture. In short, the idea is to transform the images into the PY domain, and subsequently apply the CNN. As outlined in Proposition E.1

in Section E.4, the operation in question can be described by transforming the (calibrated) image coordinates according to $\phi_{\text{pol}}(\tan(r), \varphi) \mapsto \phi_{\text{pol}}(r, \varphi - \frac{\pi}{2})$. In practice, we disregard the resulting image plane rotation by $-\frac{\pi}{2}$, resulting in a purely non-linear rescaling of the radius according to $\tan(r) \mapsto r$. Finally, we transform our image into pixel coordinates by applying an affine transformation in each of the coordinates. These are chosen such that the transformed image has the same size as the original image, while including as few pixels where the image is undefined as possible. Note that in our special setting, where all images in the database are taken by the same camera (or very at least very similar in the CMU case), this amounts to sampling all PY-images on a common 'exhausting' grid in PY-space. For more diverse datasets, more care needs to be taken to achieve this.

The pixels in which the the resulting images is undefined are simply set to zero. The object segmentation masks are transformed along with the images, effectively resulting in a transformation of the resulting bounding boxes as well. A graphical description of the procedure is given by Figure 7. In order to increase readability, we will refer to this procedure as warping the image.

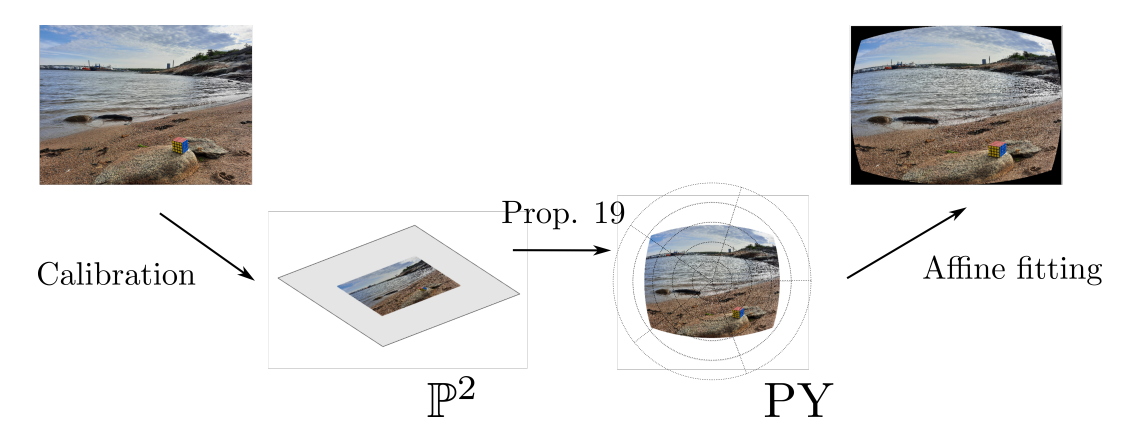


Figure 7: Transforming (warping) a \mathbb{P}^2 -image represented in the pixel domain to a PY-image in the pixel domain.

In addition to transforming the images, we also make a couple of adjustments to the prediction targets, with the purpose of making the learning task suitable for the PY-equivariant setting. The labels are rigid motions $(R,t) \in SO(3) \times \mathbb{R}^3$, which describe the pose of the objects relative to the camera coordinate system. Each translation target $t \in \mathbb{R}^3$ (the position of an object in the camera frame) is transformed to (α, s) , where $\alpha \in PY$ is the warped version of $\pi(t)$, and $s = |t| \in \mathbb{R}$ is the camera-to-object distance. As compared to t_2 , we believe the distance of camera to object is a more fitting target for the approximate spherical camera model in our approach. To be precise, while for a standard pinhole camera the object appearance in the image (in particular, its size) is roughly determined by t_2 , this is not the case for a spherical camera. In this case, the camera-to-object distance is instead the corresponding determining factor.

Note that the new representation shares some properties with [10]: The authors of that article also decouple the prediction of t_0 , t_1 from the depth t_2 . Rather than predicting the coordinates t_0 t_1 directly, an offset is predicted from the center of an anchor box to the projection of t in the image. Our adjustments for the PY case are consistent with this, with the difference that both anchor box centers and t projections are expressed in the PY-domain, and consequently the offsets as well.

Similarly, we argue that in the PY case, the object orientation $R \in SO(3)$ should not be expressed as a rotation relative to the camera frame. Instead, we define a pixel-dependent frame of reference S for rotation estimation. Such a coordinate frame is given by taking the camera frame, and rotating it such that the x_2 axis, previously aligned with the optical axis, now aligns with the viewing ray corresponding to the pixel. Such a rotation is of course not uniquely determined; we use the one of the form $\exp(\alpha)$, $\alpha \in PY$, with $|\alpha|$ minimal. The adjustment of the rotation target is motivated by the fact that an object's appearance in PY is roughly invariant to rotations around the camera (only translated), and should only be inferred relative to such a varying frame. There is further evidence in the literature supporting this choice. In [35] the same rotation targets as we propose are used with success for 3D object reconstruction.

Some small experiments empirically verifying that our modifications are appropriate can be found in Section F.1.1.

B.1.2 Image rescale augmentation

EfficientPose proposes a delicate way to scale-augment 6D-pose data. When scaling the image by a factor f, the authors propose to scale the target depth coordinates t_2 by the factor $\frac{1}{f}$ (effectively modeling an x_2 -translation), as an object farther away (f < 1) will appear smaller in the image (and vice versa). As the authors of [10] point out, this is an approximation, which will introduce an error unless t_2 accurately describes a constant depth for the whole visible object surface. Occlusion effects can also arise, especially for objects far from the center of the image.

Likewise, we adopt an approximate scaling augmentation procedure to our setting as follows. Recall that the pose labels are of the form $(R, \alpha, s) \in SO(3) \times PY \times \mathbb{R}$. When we scale a point $(x, y) \in \mathbb{P}^2$ negatively, it will move towards the center of the image. To mimic this behaviour, we choose to transform $(\alpha, s) \in PY \times \mathbb{R}$ to $(f\alpha, s/f) \in PY \times \mathbb{R}$. In this manner, moving the object away from the camera (f < 1) will result in a shift of the object towards the image center. The shift in PY-coordinates is hence equal to $\alpha(f - 1)$.

This means, approximately, that we rotate the object according to $\exp(\alpha(f-1))$. We therefore adjust the rotation R relative to the camera coordinate system according to $R \mapsto \exp(\alpha(1-f))R$.

B.1.3 Rotational homography data augmentation

Let us describe the details of the augmentations as described in Section 4. Note that three different augmentations are performed: Scalings, rotations in the image plane (referred to as rolls) and homographies corresponding to pitch-yaw rotations $\exp(\alpha)$ for $\alpha \in PY$. The scalings are applied as described in the previous section, with the f parameter uniformly sampled between 0.7 and 1.3, i.e. just as in [10]. The rolls are sampled uniformly in either $[-45^{\circ}, 45^{\circ}]$ or $[-180^{\circ}, 180^{\circ}]$. As for the tilt, we sample the radius of the α -parameter uniformly in $[0, 20^{\circ}]$, and the direction in the unit plane uniformly over the unit circle.

All three augmentations are combined into one single homography H, in order to reduce interpolation errors and truncation effects.

B.1.4 Non-geometric augmentations

In addition to the geometric augmentations described above, the same color-space augmentations as in [10] are applied. These are essentially the ones given by the RandAugment-function of the imgaug-package [32], however only including the augmentations in the color space, i.e. excluding crops, rotations, shears etc.

B.1.5 Further changes to the code

In difference to [10], we reshuffle the data between epochs, and only record the performance of the last model, and thus do not cherry-pick the best performing epoch. These changes are applied for all experiments, including the baseline, to facilitate a fair comparison.

B.1.6 Hyperparameters

We use essentially the same hyperparameters as [10], with a notable exception for the $\phi = 0$ experiments. These used a learning rate of $3 \cdot 10^{-4}$, instead of 10^{-4} , and a batch size of 6, instead of 1. This change was only made to speed up the experiments. Furthermore, we explored a moderation of the range of 'roll' augmentation from a maximum of 180 degrees to 45 degrees, and applied this moderation for all RH_{aug} experiments with the small $\phi = 0$ model, unless mentioned otherwise. We have made no further hyperparameter modifications as compared to the original implementation.

We initialize with pretrained parameters of an EfficientDet model [53] trained on COCO [40], and train with the Adam optimizer, using gradient norm clipping with 10^{-3} threshold, and a learning rate decay schedule, all consistent with [10]. The number of training epochs depends on the fraction of data used – we scale up the number of epochs for low data fractions in order to have enough training iterations for the loss to converge. For the full data we run 5k epochs, as did Bukschat and Vetter. For the 20, 35 and 80 images cases we run 10k epochs and for the 130 image case we run 7k epochs. We cap the epoch number at 10k as it seems to suffice for convergence in all cases. Validation is carried out every 50 epochs for the Occlusion LINEMOD experiments, and every 100 epochs for LINEMOD.

B.1.7 Hardware and runtime

We use two computing setups. Initial Occlusion LINEMOD experiments were carried out with Tensorflow 1.15 in a Docker container running Ubuntu 18.04, on a workstation with host operating system Manjaro. The hardware

has 64 GB RAM, a 6-core Intel Core i7-8700K CPU, and an Nvidia GTX 1080 Ti GPU with 11GB memory. The LINEMOD experiments use the same Docker container¹, but these experiments involve many training cycles since a separate model is trained for each object, and therefore computations are carried out on a compute cluster. Further runs of the Occlusion LINEMOD experiments are also carried out on the compute cluster in the same way. Each compute node is running CentOS 7 and is equipped with 72GB RAM, four CPU cores of type Intel(R) Xeon(R) Gold 6226R CPU @ 2.90GH, and an Nvidia Tesla T4 GPU with 16GB memory. Training takes around 24 hours for each Occlusion LINEMOD model, and around 30 hours for each LINEMOD model.

B.2 DSAC*

Our visual localization experiments on 7-scenes build on DSAC* [8], and the code supplied at [9].

The first step of the DSAC* pipeline for RGB-input is using a CNN to predict scene coordinates for each pixel in the input image in order to obtain a dense map of 2D-3D correspondences, which are then fed into DSAC [6] (a differentiable modification of RANSAC [24]) with a PnP solver for estimation of the camera pose. At test time, standard RANSAC is used instead of DSAC. Lastly, the estimated camera pose is iteratively refined to maximize the number of inlier correspondences.

Training of the CNN parameters in DSAC* consists of two phases, first training the CNN to output reasonable 3D coordinates with a loss on the reprojection of the predicted scene coordinates and finally training end to end using DSAC and the PnP solver with a loss on the camera pose. We refer to [8] for the precise formulations of the loss functions.

The differences between our five experiment setups as listed in Section 5.2 are summarized in Table 4.

	Image	Image		
Experiment	domain	scalings	Rolls (°)	Tilts (°)
Baseline	\mathbb{P}^2	None	None	None
Baseline+GeomAug	\mathbb{P}^2	[2/3, 3/2]	[-30, 30]	None
$\mathrm{RH}_{\mathrm{aug}}$	\mathbb{P}^2	[2/3, 3/2]	[-30, 30]	[0, 20]
PY	PY	None	None	None
PY+GeomAug	PY	[2/3, 3/2]	[-30, 30]	None

Table 4: The experiment settings for visual localization on 7-Scenes with DSAC* Tiny. Rolls and tilts are defined in Section B.1.3. When an interval is specified, we sample a value in the interval for each training image in each epoch.

B.2.1 Data augmentation

Except for the experiment with general rotational homographies (RH_{aug}), the augmentation procedure follows the one in [8], which in turn is inspired by the augmentation procedure in [38].

All experiments use color jitter data augmentation during both training phases, by which we mean randomly rescaling the brightness and contrast of an image within $\pm 10\%$.

Geometric data augmentation. For simplicity, we use geometric data augmentation only during the first training phase, which consists of 10 times more epochs than the second training phase.

In the experiments denoted "+GeomAug", we augment the training data as described in [8] by randomly rotating the images in the range of ± 30 degrees in the image plane and rescaling the image by a random factor between 2 /3 and 3 /2. The ground truth camera pose is altered according to the rotation and the camera calibration according to the rescaling.

RH data augmentation. The RH augmentation is conducted just as for EfficientPose (see Section B.1.3). It is only applied during the first training phase.

B.2.2 Transformation to PY

For the experiments called PY, we transform the input image to the PY-domain and retransform the CNN output to the original \mathbb{P}^2 -domain before feeding the correspondences into DSAC. This approach was the simplest as the

¹However, the Docker container is here converted to a Singularity container due to system constraints.

DSAC implementation bundled with DSAC* uses a dense prediction of 2D-3D correspondences relating every pixel in an (subsampled) image to a scene coordinate.

The transformation to the PY-domain proceeds just as in the experiments with EfficientPose, see Section B.1.1. Transforming back is done similarily, for every pixel in the subsampled image we calculate its PY-coordinates and bilinearly interpolate the scene coordinate from the output of the CNN which is in the PY-domain.

B.2.3 Further changes to the DSAC* code

Here we detail important changes made to the original DSAC* code that are not specific to the PY- or RH-experiments. These changes are applied to all our experiments with DSAC* Tiny.

Pixel grid. The CNN in the DSAC* Tiny model has the layout described in Figure 8. Of particular note is the fact that three layers use stride 2 convolutions, leading to a subsampling of the input image dimensions by a factor of around 8 (depending on the input image). When calculating the pixel coordinates corresponding to the predicted 3D coordinates one has to keep this fact in mind. The original DSAC* code does this by subsampling the original pixels, starting at pixel [4,4] and incrementing by 8 in the x_0 and x_1 directions until reaching the image size. However, since the convolutions are padded, we believe it to be more correct to start at pixel [0,0] and thus implement this change.

Augmentation mask. In [8], the authors state that they see deteriorated performance when using data augmentation with the low capacity DSAC* Tiny model. Out of concern for this, we add an augmentation mask to the code, so that only those pixels in an augmented image which correspond to pixel coordinates inside the original image contribute to the loss function.

B.2.4 Dataset details

We use the standard train-test-split for 7-Scenes that is provided with the dataset.

B.2.5 Hyperparameters

The CNN in DSAC* Tiny is fully convolutional, with some residual blocks. The layout is described in Figure 8. We follow [8] for hyperparameter choices and do not perform any hyperparameter optimization ourselves. For convenience we list the hyperparameters in Table 5.

	Number of	Temperature						
	RANSAC	(higher means	Max number	Initial	Initial	End-to-end	End-to-end	
Inlier	hypotheses	DSAC closer	of refinement	phase	phase	phase	phase	
threshold	sampled	to RANSAC)	iterations	learning rate	iterations	learning rate	iterations	Optimizer
$\tau = 10 \mathrm{px}$	M = 64	$\alpha = \frac{100}{\text{nbr. correspondences}}$	100	10-4	106	10-6	10 ⁵	Adam

Table 5: The hyperparameter settings for visual localization on 7-Scenes with DSAC* Tiny [8]. These are the same for all experiments.

B.2.6 Hardware and runtime

We train all models on the same kind of cluster compute nodes as described in Section B.1.7, but with a Singularity container running Debian 10, and with Pytorch 1.6 installed. The initial training phase takes around 7 hours and the end-to-end training phase takes around 8 hours.

B.3 Pixloc

Our visual localization experiments on the CMU Extended seasons dataset build on Pixloc [46] as explained in A.1. In the undistorted, PY-warp and RH-augment experiments we undistort, warp and/or augment both the query and reference images and modify the corresponding cameras accordingly. In both the warp and augment cases we undistort the image prior to further processing. We also change which 3D points should be considered for projections into the images according to the new cameras. We implement the derivative for the warp projection to enable the Levenberg-Marquardt method used in Pixloc.

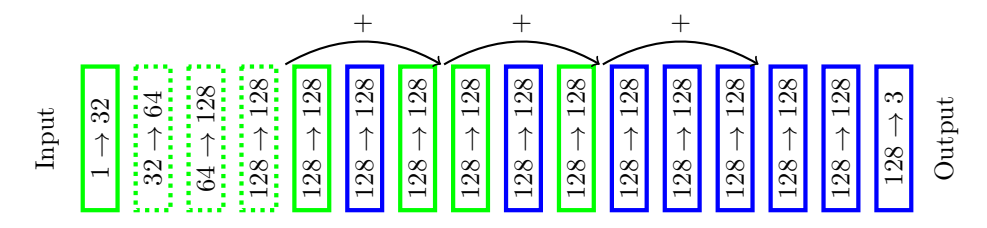


Figure 8: The CNN in DSAC* Tiny [8]. The network takes a single grayscale image as input and outputs 3D coordinates corresponding to 2D pixels in a subsampled image. The green layers consist of 3×3 -convolutions and the blue layers of 1×1 -convolutions. Between consecutive convolution layers, there are ReLU activations. The notation in the boxes means "number of input channels \rightarrow number of output channels". Skip connections are shown by the arrows marked with +. The dotted layers use convolution with stride 2, while all others use stride 1. Every 3×3 -convolution uses padding of one pixel around the image.

B.3.1 RH-augmentations

The RH-augmentations are carried out on undistorted images, as they do not make sense on radially distorted images. Because the pose of the found reference image for a given query image is often quite close in rotation to the query, we use small augmentations: rolls sampled uniformly from $[-1^{\circ}, 1^{\circ}]$ and tilts around a random axis in the camera plane of size uniformly sampled from $[-5^{\circ}, 5^{\circ}]$. In the RH_{aug} + PY case we first undistort the images, then augment them and finally warp them to PY.

B.3.2 Data details

We use the training-validation split supplied by the Pixloc authors. There are 9 training slices. The full training data consists of $N_{\rm max}=191456$ query-ref pairs but in each epoch only 1000 from each CMU training slice are used (randomly sampled), yielding 9000 pairs (this follows the training procedure used by Sarlin et al.). The other data proportions 4^{-k} have approximately $4^{-k}N_{\rm max}$ ref-query pairs in total (approximately because we subsample the number of query images rather than the number of query-ref pairs), from which also 1000 per slice are sampled whenever the available amount is larger than 1000. For instance, at the proportion $4^{-5}\approx 10^{-3}$, only 209 pairs are available in total and these were used in every epoch.

B.3.3 Training details

We use the same hyperparameters as Sarlin et. al., except for the fact that we explicitly stop the training after 45k iterations or 200 epochs (which one is earlier depends on the data proportion) – Sarlin et. al. suggest manually braking the training after the validation loss has converged at around "30k-40k" iterations. We find that simply breaking at 45k iterations or 200 epochs works well. Of note is that the batch size of 3 means that 45k iterations corresponds to going through $3 \cdot 45000 = 135000$ query-ref pairs. This is lower than the total available amount in the full data case and in the $4^{-1} = 0.25$ and $4^{-2} \approx 0.063$ proportion cases it means that the available data is not passed through many times during training, giving a possible explanation of the similar performance of these proportions to the full data case.

B.3.4 Hardware and runtime

The models are trained on the same kind of cluster compute nodes as described in Section B.1.7, but with a Singularity container running Debian 10 with Python 3.9 and Pytorch 1.10. The training takes around 48 hours.

C A group action of PY on $\mathbb{N} \times \mathbb{S}^2$

Here, we describe how an action of PY on $\mathbb{N} \times \mathbb{S}^2$ can be constructed. Recall that an action of a group G on a set K is a map $\chi: G \times K \to K, (g,k) \mapsto \chi_g(k)$ with the property that $\chi_g(\chi_h(k)) = \chi_{gh}k$.

The action should fulfill satisfy $\chi_{\alpha}(e_2) = \exp(\alpha)e_2$, at least for small α , in order to resemble the SO(3)-action of the pitch-yaw $\exp(\alpha)$ as good as possible close to e_2 . A natural ansatz for the group action would be, defining the map $\Psi : \text{PY} \to \mathbb{S}^2$ through $\Psi(\alpha) = \exp(\alpha)e_2$, the following formula:

$$\chi_{\beta}(\theta) = \Psi(\beta + \Psi^{-1}(\theta)),$$

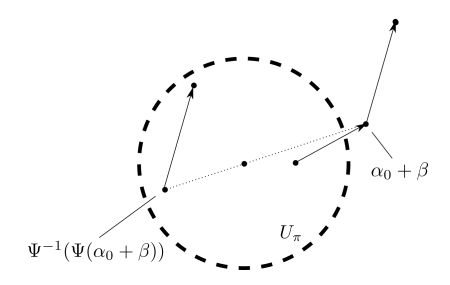


Figure 9: $\Psi^{-1}(\Psi(\alpha_0 + \beta)) + \gamma \neq \alpha_0 + \beta + \gamma$

where the inverse is the inverse of the restriction of Ψ on U_{π} . However, this is *not* a group action. To see this, note that, excluding the circles of radius $n\pi, n \in \mathbb{N}$ around the origin, the map $\Psi^{-1} \circ \Psi$ maps α to the unique element on the line

$$\ell_{\alpha} = \{ \beta \mid \beta \text{ collinear with } \alpha, |\beta| - |\alpha| \in 2\pi \mathbb{Z} \}$$

which lies inside U_{π} . Hence, for $\theta = \Psi(\alpha_0)$ with $\alpha_0 \in U_{\pi}$, $\Psi^{-1}(\chi_{\beta}(\theta)) = \Psi^{-1}(\Psi(\alpha_0 + \beta)) \neq \alpha_0 + \beta$ for many β . In fact, for such α_0 and β , we will even for most values for γ have $\gamma \neq \alpha_0 + \beta + \gamma$ (see Figure 9). Hence,

$$\chi_{\gamma}(\chi_{\beta}(\alpha_0)) = \Psi(\gamma + \Psi^{-1}(\chi_{\beta}(\theta))) = \Psi(\gamma + \Psi^{-1}(\Psi(\alpha_0 + \beta))) \neq \Psi^{-1}(\gamma + \alpha_0 + \beta) = \chi_{\gamma + \beta}(\theta)$$

This explains why need to define a map on PY with better bijectivity properties. This is possible if we extend the range to $\mathbb{N} \times \mathbb{S}^2$.

Proposition C.1. For $[\alpha] \in PY$, we consider the curve $\gamma : [0,1] \to \mathbb{S}^2, t \mapsto \exp(t\alpha)e_2$. Letting n be the number of times γ crosses the set $\{\pm e_2\}$, we define a map $\Phi : PY \to \mathbb{N} \times \mathbb{S}^2$ through

$$\Phi(\alpha) := (n, \gamma(1)).$$

Then, Φ is injective on PY, excluding circles of radius of multiples of π around 0.

To prove this lemma, let us first show that $\gamma(t) = \exp(\alpha t)$ defines a geodesic.

Lemma C.2. For $\alpha \in PY$, $\gamma : \mathbb{R} \to \mathbb{S}^2$, $t \mapsto \exp(t\alpha)e_2$ is a geodesic with speed $|\alpha|$ and $\gamma'(0) = \alpha e_2$.

Proof. Due to the properties of the matrix exponential map, the first two extrinsic derivatives of γ are given by

$$\gamma'(t) = \alpha \exp(\alpha t)e_2, \quad \gamma''(t) = \alpha^2 \exp(\alpha t)e_2.$$

This already proves that $\gamma'(0) = \alpha e_2$. To show that γ is a geodesic, we now only need to argue that $\gamma''(t)$ is perpendicular to the tangent plane at each point $\gamma(t)$. For the sphere, this simply means that $\gamma''(t)$ should be parallel with $\gamma(t)$. However, since α commutes with $\exp(\alpha)$, we get

$$\gamma''(t) = \alpha^2 \exp(\alpha t) e_2 = \exp(\alpha t) \alpha^2 e_2 = |\alpha|^2 \exp(\alpha t) e_2 = -|\alpha|^2 \gamma(t),$$

where the penultimate step is the result of a simple computation. The proof is finished.

Proving Lemma C.1 is now easy.

Proof of Prop. C.1. Due to Lemma C.2, we know that for each α , γ is a geodesic with speed $|\alpha|$. Therefore, it traverses along a great circle which goes through e_2 . This great circle is uniquely determined by $\gamma(1)$, unless $|\alpha|$ is a multiple of π , which we excluded. Thus, if two elements have the same image under Φ , the corresponding curves must have traversed along the same great circles. The only way they could have ended up in the same endpoint $\gamma(1)$ is that one curve has traversed the geodesic a multiple of a half revolution of the entire sphere more times. However, since they have crossed $\{\pm e_2\}$ the same number of times, the curves must however be exactly equal, (which for instance can be seen by comparing derivatives in t=0), and therefore also the endpoints.

Using Φ , the action may now (excluding the south poles $(n, -e_2), n \in \mathbb{N}$) be defined as follows

$$\chi_{\beta}(\theta) = \Phi(\beta + \Phi^{-1}(\theta)).$$

Since Φ is injective, we then have $\Phi^{-1} \circ \Phi(\alpha_0 + \beta) = \alpha_0 + \beta$ for all α with $|\alpha| \neq \pi \mathbb{N}$, which prevents the problems described above from occurring.

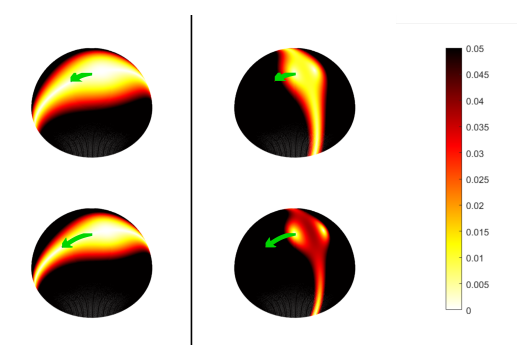


Figure 10: The distortion $|\varphi_{\alpha} - \psi_{\alpha}|$, corresponding to the PY-group (left) compared to the distortion $|\chi_{\alpha} - \psi_{\alpha}|$, corresponding to the translation group. The above plots are for a rotation of $\pi/9$ radians, the below for a rotation of $\pi/6$ radians. The respective rotations are illustrated by the green arrows, whose starting points mark $\theta = e_2$.

D Approximation property of PY

In this section we provide a formal analysis of the approximation property of the PY-group. Fix an $\alpha \in PY$. We will compare three maps

$$\psi_{\alpha}: \mathbb{S}^{2} \to \mathbb{S}^{2}, \theta \mapsto \exp(\alpha)\theta,$$

$$\varphi_{\alpha}: \mathbb{S}^{2} \to \mathbb{S}^{2}, \theta \mapsto \operatorname{pr}_{\mathbb{S}^{2}} \Phi \left(\alpha + \Phi^{-1}(0, \theta)\right),$$

$$\chi_{\alpha}: \mathbb{S}^{2} \to \mathbb{S}^{2}, \theta \mapsto \pi^{-1}(\pi(\theta) + t),$$

where t is defined via $\pi(\exp(\alpha)e_2)$, and $\operatorname{pr}_{\mathbb{S}^2}$ projects $(n,\theta) \in \mathbb{N} \times \mathbb{S}^2$ to $\theta \in \mathbb{S}^2$. Note that the inverse of π here refers to its restriction to the upper half of \mathbb{S}^2 , in formulas

$$\pi^{-1}: \mathbb{P}^2 \to \mathbb{S}^2, v \mapsto \frac{1}{\sqrt{1+|v|^2}} \begin{bmatrix} v \\ 0 \end{bmatrix}.$$

The three maps ψ_{α} , φ_{α} , χ_{α} correspond to actually applying the pitch-yaw rotation (ψ_{α}) , applying the pitch-yaw as a PY-translation (φ_{α}) , and applying the translation in the image plane such that it is translated as it would have been by the rotation and subsequent projection onto \mathbb{P}^2 (χ_{α}) .

Already comparing the plots of the functions $|\varphi_{\alpha} - \psi_{\alpha}|$ and $|\chi_{\alpha} - \psi_{\alpha}|$ in Figure 10, we see that the PY-translation φ_{α} is much better at approximating the rotation ψ_{α} than the translation χ_{α} . In the following, we provide a theoretical analysis, which will prove additional insight.

We begin by comparing ψ_{α} and φ_{α} , i.e. the action of $\exp(\alpha)$ as an element in SO(3) and of α as a PY-translation. Proposition D.1. We have

$$|\varphi_{\alpha}(\exp(\beta)e_2) - \psi_{\alpha}(\exp(\beta)e_2)| \le \left|\frac{1}{6}[\alpha, \beta](\alpha + 2\beta)e_2\right| + \mathcal{O}(|\alpha|^3) + \mathcal{O}(|\beta|^3).$$

Here, $[\alpha, \beta]$ denotes the commutator $(\alpha\beta - \beta\alpha) \in \mathbb{R}^{3,3}$.

Proof. We have $\varphi_{\alpha}(\exp(\beta)) = \Phi(\alpha + \beta) = \exp(\alpha + \beta)e_2$. Thus, what we need to estimate is

$$\exp(\alpha + \beta)e_2 - \exp(\alpha)\exp(\beta)e_2.$$

We have the following Taylor-expansion of exp around 0

$$\exp(\beta) = \mathrm{id} + \beta + \frac{1}{2}\beta^2 + \mathcal{O}(|\beta|^3).$$

We can also Taylor-expand exp around α to obtain

$$\exp(\alpha + \beta) = \exp(\alpha) + \exp'(\alpha)\beta + \frac{1}{2}\exp''(\alpha)(\beta, \beta) + \mathcal{O}(|\beta|^3).$$

We now need to calculate these derivatives. For this, we use the following formula (see eq. 3 in [44])

$$\exp^{(k)}(t\alpha)(t\beta)^k = k \cdot \exp(t\alpha) \int_0^t \exp(-s\alpha)\beta \exp^{(k-1)}(s\alpha)(s\beta)^{k-1} ds, \quad \exp^{(0)}(t\alpha) = \exp(t\alpha).$$

Let us begin by investigating the first derivative. Since

$$\exp(-s\alpha)\beta \exp(s\alpha) = \left(id - s\alpha + \frac{s^2}{2}\alpha^2 + \mathcal{O}(s^3 |\alpha|^3)\right)\beta \left(id + s\alpha + \frac{s^2}{2}\alpha^2 + \mathcal{O}(s^3 |\alpha|^3)\right)$$

$$= \beta - s[\alpha, \beta] + \frac{s^2}{2}[\alpha, [\alpha, \beta]] + \mathcal{O}(|\alpha|^3)$$
(3)

we get by carrying out the integration

$$\exp'(t\alpha)t\beta = \exp(t\alpha)\left(t\beta - \frac{t^2}{2}[\alpha, \beta] + \frac{t^3}{6}[\alpha, [\alpha, \beta]] + \mathcal{O}(|\alpha|^3)\right). \tag{4}$$

We may now use this to estimate the second derivative

$$\frac{1}{2}\exp''(\alpha)(\beta,\beta) = \exp(\alpha) \int_{0}^{1} \exp(-s\alpha)\beta \exp'(s\alpha)s\beta ds$$

$$= \exp(\alpha) \int_{0}^{1} \exp(-s\alpha)\beta \exp(s\alpha) \left(s\beta - \frac{1}{2}s^{2}[\alpha,\beta] + \frac{s^{3}}{6}[\alpha,[\alpha,\beta]]\right) ds$$

$$+ \mathcal{O}(|\alpha|^{3})$$

$$= \exp(\alpha) \int_{0}^{1} s\beta^{2} - \frac{s^{2}}{2}(\beta[\alpha,\beta] + 2[\alpha,\beta]\beta)$$

$$+ \frac{s^{3}}{6}(\beta[\alpha,[\alpha,\beta]] + 3[\alpha,[\alpha,\beta]]\beta + 3[\alpha,\beta]^{2}) + \mathcal{O}(|\alpha|^{3}) ds$$

$$= \exp(\alpha) \left(\frac{1}{2}\beta^{2} - \frac{1}{6}(\beta[\alpha,\beta] + 2[\alpha,\beta]\beta)$$

$$+ \frac{1}{24}(\beta[\alpha,[\alpha,\beta]] + 3[\alpha,[\alpha,\beta]]\beta + 3[\alpha,\beta]^{2}) + \mathcal{O}(|\alpha|^{3})\right) \tag{5}$$

where we again used (3) in the penultimate step. Using (4) and (5), we get that the difference $\exp(\alpha + \beta) - \exp(\alpha) \exp(\beta)$ equals

$$\begin{split} \exp(\alpha) \bigg(&- \tfrac{1}{2} [\alpha, \beta] + \tfrac{1}{6} [\alpha, [\alpha, \beta]] - \tfrac{1}{6} \left(\beta [\alpha, \beta] + 2[\alpha, \beta] \beta\right) \\ &+ \tfrac{1}{24} \left(\beta [\alpha, [\alpha, \beta]] + 3[\alpha, [\alpha, \beta]] \beta + 3[\alpha, \beta]^2\right) + \mathcal{O}(|\alpha|^3) + \mathcal{O}(|\beta|^3) \bigg) \end{split}$$

We now need to remember that we are not looking for an estimate of the matrices, but rather their action on e_2 . The commutator $[\alpha, \beta]$ must be a multiple of C_2 , the matrix that represents the linear map $v \mapsto e_2 \times v$. As such,

$$[\alpha, \beta]e_2 = 0.$$

for all $\alpha, \beta \in PY$. Using this, the above simplifies to

$$\exp(\alpha) \left(-\frac{1}{6} [\alpha, \beta] (\alpha e_2 + 2\beta e_2 - \frac{3}{4} \alpha \beta e_2) + \frac{1}{24} (-\beta [\alpha, \beta] \alpha e_2 + 3\alpha [\alpha, \beta] \beta e_2 \right) + \mathcal{O}(|\alpha|^3) + \mathcal{O}(|\beta|^3).$$

Now, it is a straightforward calculation to show that $\alpha\beta e_2 \in \text{span}(e_2)$. As such, we must have $[\alpha, \beta]\alpha\beta e_2 = 0$. This, together with $[\alpha, \beta]e_2 = 0$, yields $\alpha\beta\alpha\beta e_2 = \beta\alpha\beta\alpha e_2$. Using this, and the fact that $\alpha^2\beta^2 e_2 = \beta^2\alpha^2 e_2 = |\alpha|^2 |\beta|^2 e_2$, finally shows that

$$\beta[\alpha,\beta]\alpha e_2 = \beta\alpha\beta\alpha e_2 - \beta^2\alpha^2 e_2 = -(\alpha^2\beta^2 - \beta\alpha\beta\alpha)e_2 = -\alpha[\alpha,\beta]\beta e_2.$$

The error thus equals

$$-\frac{1}{6}\exp(\alpha)([\alpha,\beta](\alpha e_2 + 2\beta e_2) + \beta[\alpha,\beta]\alpha e_2) + \mathcal{O}(|\alpha|^3) + \mathcal{O}(|\beta|^3).$$
(6)

Now notice that

$$\exp(\beta)[\alpha, \beta](\alpha + 2\beta) = (\mathrm{id} + \beta)[\alpha, \beta](\alpha + 2\beta) + \mathcal{O}(|\beta|^3)$$
$$= [\alpha, \beta](\alpha + 2\beta) + \beta[\alpha, \beta]\alpha + \mathcal{O}(|\beta|^3).$$

Hence, (6) simplifies to

$$-\frac{1}{6}\exp(\alpha)\left(\exp(\beta)[\alpha,\beta](\alpha+2\beta)+\mathcal{O}(|\alpha|^3)+\mathcal{O}(|\beta|^3)\right)$$

which, together with the fact that $\exp(\alpha)$ and $\exp(\beta)$ are orthogonal matrices, yields the claim.

Notice the $[\alpha, \beta]$ -term appearing in the error. This term is identically equal to zero for β parallel with α . This means that close to the great circle $t \mapsto \exp(\alpha t)$, the distortion of PY-translating with α compared with performing the actual rotation $\exp(\alpha)$ is especially small. In fact, it is not hard to show that on that great circle, $\psi_{\alpha} = \varphi_{\alpha}$.

Proposition D.2. On the great circle $t \mapsto \exp(t\alpha)$, φ_{α} and ψ_{α} , as defined in Proposition D.1, are equal.

Proof. We need to compare $\varphi_{\alpha}(\exp(t\alpha)) = \exp(\alpha + t\alpha)e_2$ and $\psi_{\alpha}(\exp(\alpha t)) = \exp(\alpha)\exp(t\alpha)e_2$. It is however well-known that $\exp(\alpha + \beta) = \exp(\alpha)\exp(\beta)$ if α and β commute, which α and $t\alpha$ surely do. This in particular implies $\varphi_{\alpha}(\exp(\alpha t)) = \exp(\alpha + t\alpha)e_2 = \exp(\alpha)\exp(t\alpha)e_2 = \psi_{\alpha}(\exp(\alpha t))$, i.e., the statement.

We move on to the comparison of ψ_{α} and χ_{α} .

Proposition D.3. Let π be the projection $\mathbb{S}^2_+ \to \mathbb{P}^2$, $\alpha \in \mathrm{PY}$ and t be defined via $t = \pi(\exp(\alpha)e_2)$

$$\chi_{\alpha}: \mathbb{S}^2 \to \mathbb{S}^2, \theta \mapsto \pi^{-1}(\pi(\theta) + t)$$

Then

$$\chi_{\alpha}(\theta) - \psi_{\alpha}(\theta) = -\langle t, \theta \rangle (t + \widehat{\theta}) - \frac{1}{2} \langle \theta, \alpha \rangle \alpha + (\theta_2 - 1) \frac{|t|^2}{2} e_2 + \mathcal{O}(|t|^3) + \mathcal{O}(d_{\mathbb{S}}(\theta, e_2)^3)$$

where $\langle \cdot, \cdot \rangle$ denotes scalar product, ψ_{α} is as in Proposition D.1, $\widehat{\theta}$ the projection of θ onto span (e_0, e_1) and we identified the two-dimensional vectors α and t as three-dimensional vectors in span (e_0, e_1) .

Proof of Proposition D.3. Let us begin by relating α to t. By Taylor-expanding π^{-1} in 0 (viewing it as a function $\mathbb{P}^2 \to \mathbb{R}^3$), we obtain

$$\pi^{-1}(t) = \pi^{-1}(0) + \begin{bmatrix} t \\ 0 \end{bmatrix} - \frac{|t|^2}{2}e_2 + \mathcal{O}(|t|^3) = e_2 + \begin{bmatrix} t \\ 0 \end{bmatrix} - \frac{|t|^2}{2}e_2 + \mathcal{O}(|t|^3).$$

Comparing this to

$$\exp(\alpha)e_2 = e_2 + \alpha e_2 + \frac{1}{2}\alpha^2 e_2 + \mathcal{O}(|\alpha|^3) = e_2 + \alpha e_2 - \frac{|\alpha|^2}{2}e_2 + \mathcal{O}(|\alpha|^3)$$

we see that $\exp(\alpha)e_2 = \pi^{-1}(t)$ implies that

$$t = \alpha e_2 + \mathcal{O}(|\alpha|^3) = \begin{bmatrix} \alpha_1 \\ -\alpha_0 \\ 0 \end{bmatrix} + \mathcal{O}(|\alpha|^3). \tag{7}$$

Now, Taylor-expanding π^{-1} in t and disregarding all terms which have a least order 3 in t or v, we obtain

$$\pi^{-1}(t+v) = \pi^{-1}(t) - \left(\langle t, v \rangle + \frac{|v|^2}{2}\right) \begin{bmatrix} t \\ 1 \end{bmatrix} + \left(1 - \frac{|t|^2}{2} - \langle t, v \rangle - \frac{|v|^2}{2}\right) \begin{bmatrix} v \\ 0 \end{bmatrix} + \mathcal{O}_t(|v|^3) + \mathcal{O}(|t|^3)$$

We want to replace v with $\pi(\theta)$. Performing an expansion of this function around e_2 yields

$$\pi(\theta) = 0 + \widehat{\theta} + (1 - \theta_2)\widehat{\theta} + \mathcal{O}(d_{\mathbb{S}}(e_2, \theta)^4) = \widehat{\theta} + \mathcal{O}(d_{\mathbb{S}}(e_2, \theta)^3).$$

Hence,

$$\pi^{-1}(t+\pi(\theta)) = \exp(\alpha)e_2 - \left(\langle t, \widehat{\theta} \rangle + \frac{|\widehat{\theta}|^2}{2}\right) \begin{bmatrix} t \\ 1 \end{bmatrix} + \left(1 - \frac{|t|^2}{2} - \langle t, \widehat{\theta} \rangle\right) \begin{bmatrix} \widehat{\theta} \\ 0 \end{bmatrix}$$

$$+ \mathcal{O}(d_{\mathbb{S}}(e_2, \theta)^3) + \mathcal{O}(|t|^3).$$

$$= \exp(\alpha)e_2 + \begin{bmatrix} \widehat{\theta} \\ 0 \end{bmatrix} - \langle t, \widehat{\theta} \rangle \begin{bmatrix} t + \widehat{\theta} \\ 1 \end{bmatrix} - \frac{|\widehat{\theta}|^2}{2} \begin{bmatrix} t \\ 1 \end{bmatrix} - \frac{|t|^2}{2} \begin{bmatrix} \widehat{\theta} \\ 0 \end{bmatrix}$$

$$+ \mathcal{O}(d_{\mathbb{S}}(e_2, \theta)^3) + \mathcal{O}(|t|^3).$$

This is to be compared to $\exp(\alpha)\theta$, i.e.

$$\exp(\alpha)\theta = \exp(\alpha)e_2 + (\mathrm{id} + \alpha + \frac{1}{2}\alpha^2 + \mathcal{O}(|\alpha|^3))(\theta - e_2)$$

Using (7), we obtain

$$\begin{aligned} (\mathrm{id} + \alpha + \tfrac{1}{2}\alpha^2)(\theta - e_2) &= \begin{bmatrix} \widehat{\theta} \\ \theta_2 - 1 \end{bmatrix} + \begin{bmatrix} t(\theta_2 - 1) \\ -\langle t, \widehat{\theta} \rangle \end{bmatrix} - \tfrac{|t|^2}{2} \begin{bmatrix} \widehat{\theta} \\ \theta_2 - 1 \end{bmatrix} + \tfrac{1}{2}\langle \widehat{\theta}, \alpha \rangle \begin{bmatrix} \alpha \\ 0 \end{bmatrix} + \mathcal{O}(|\alpha|^3) \\ &= \begin{bmatrix} \widehat{\theta} \\ 0 \end{bmatrix} + (\theta_2 - 1) \begin{bmatrix} t \\ 1 \end{bmatrix} - \langle t, \widehat{\theta} \rangle e_2 - \tfrac{|t|^2}{2} \begin{bmatrix} \widehat{\theta} \\ \theta_2 - 1 \end{bmatrix} + \tfrac{1}{2}\langle \widehat{\theta}, \alpha \rangle \begin{bmatrix} \alpha \\ 0 \end{bmatrix} + \mathcal{O}(|\alpha|^3) \end{aligned}$$

Remembering that $\theta_2 - 1 = \frac{|\widehat{\theta}|^2}{2} + \mathcal{O}(d_{\mathbb{S}}(\theta, e_2)^4)$, we hence get

$$\chi_{\exp(\alpha)}(\theta) - \exp(\alpha)\theta = -\langle t, \widehat{\theta} \rangle \begin{bmatrix} t + \widehat{\theta} \\ 0 \end{bmatrix} + \frac{1}{2} \langle \widehat{\theta}, \alpha \rangle \begin{bmatrix} \alpha \\ 0 \end{bmatrix} - \frac{|t|^2}{2} (\theta_2 - 1) e_2 + \mathcal{O}(d_{\mathbb{S}}(e_2, \theta)^3) + \mathcal{O}(|t|^3)$$

We may safely insert a term $-\langle t, \widehat{\theta} \rangle (\theta_2 - 1)e_2$, since it is of order 3 in $d_{\mathbb{S}}(e_2, \theta)$. Also, since $t \in \text{span}(e_0, e_1)$, $\langle t, \widehat{\theta} \rangle = \langle t, \theta \rangle$. The proof is finished.

We see that this error term gets particularly small for θ perpendicular to t (at least for small t), meaning that it is small perpendicular to the translation direction. This is in contrast to the PY-induced distortion, which is smallest along the direction of the rotation. The expression as an additional sweet-spot around $\widehat{\theta} \approx -t$ the first two error terms vanish there. In fact, this can be precisized.

Proposition D.4. For $\omega = \pi^{-1}(-t)$, $\chi_{\alpha}(\omega) = \psi_{\alpha}(\omega)$.

Proof. It is a straighforward calculation to show that

$$\chi_{\alpha}(\omega) = \pi^{-1}(\pi(\omega) + t) = \pi^{-1}(-t + t) = e_2.$$

Thus, we need to show that $\psi_{\alpha}(\omega) = \exp(\alpha)\omega = e_2$, or equivalently $-t = \pi(\exp(-\alpha)e_2)$. To prove this, it suffices to show that $\langle e_j, \exp(-\alpha)e_2 \rangle = -\langle e_j, \exp(\alpha)e_2 \rangle$ for j = 0, 1 and $\langle e_2, \exp(-\alpha)e_2 \rangle = \langle e_2, \exp(\alpha)e_2 \rangle$. For this, notice that $\alpha^n e_2$ is in $\operatorname{span}(e_2)$ for n even and in $\operatorname{span}(e_0, e_1)$ for n odd (this can for instance be shown via induction). This has the consequence that for j = 0, 1

$$\langle e_j, \exp(-\alpha)e_2 \rangle = \sum_{n \in \mathbb{N}} \frac{1}{n!} \langle e_j, (-\alpha)^n e_2 \rangle = \sum_{n \text{ odd}} \frac{1}{n!} \cdot (-1)^n \langle e_j, \alpha^n e_2 \rangle = \sum_{n \text{ odd}} -\frac{1}{n!} \cdot \langle e_j, \alpha^n e_2 \rangle$$
$$= -\sum_{n \in \mathbb{N}} \frac{1}{n!} \langle e_j, \alpha^n e_2 \rangle = -\langle e_j, \exp(\alpha)e_2 \rangle,$$

and similarly $\langle e_2, \exp(-\alpha)e_2 \rangle = \langle e_2, \exp(\alpha)e_2 \rangle$. The proof is finished.

Both by looking at the error terms in Proposition D.3 and on Figure 10, we see that the translation-distortion does not have the 'sweet great circle' the PY-distortion has. To some extent it has a sweet area on another great circle though, as the final proposition shows.

Proposition D.5. On the set $G = \{\theta \mid 2\langle \pi(\theta), t \rangle + |t|^2 = 0\} \cap \{\theta \mid \theta_2 > 0\},\$

$$\chi_{\alpha}(\theta) - \psi_{\alpha}(\theta) = \frac{1}{4}\theta_2|\alpha|^2 + \mathcal{O}(|\alpha|^3),$$

Proof. For $\theta \in G$, $|\pi(\theta)| = |\pi(\theta) + t|$. This has the consequence

$$\pi^{-1}(\pi(\theta) + t) = \frac{1}{\sqrt{1 + |\pi(\theta) + t|^2}} \begin{bmatrix} \pi(\theta) + t \\ 1 \end{bmatrix} = \frac{1}{\sqrt{1 + |\pi(\theta)|^2}} \begin{bmatrix} \pi(\theta) \\ 1 \end{bmatrix} + \frac{1}{\sqrt{1 + |\pi(\theta)|^2}} \begin{bmatrix} t \\ 0 \end{bmatrix}$$
$$= \pi^{-1}(\pi(\theta)) + \frac{1}{\sqrt{1 + |\pi(\theta)|^2}} \begin{bmatrix} t \\ 0 \end{bmatrix}$$

We have $\sqrt{1+\left|\pi(\theta)\right|^2}=\theta_2^{-1}$. This, together with (7), implies

$$\pi^{-1}(\pi(\theta) + t) = \theta + \theta_2 \cdot \alpha e_2 + \mathcal{O}(|\alpha|^3).$$

Since $\exp(\alpha) = 1 + \alpha + \frac{1}{2}\alpha^2 + \mathcal{O}(|\alpha|^3)$, we obtain, using the notation of the previous proof,

$$\chi_{\alpha}(\theta) - \psi_{\alpha}(\theta) = -\alpha \begin{bmatrix} \widehat{\theta} \\ 0 \end{bmatrix} - \frac{1}{2}\alpha^{2}\theta + \mathcal{O}(|\alpha|^{3}) = \langle t, \widehat{\theta} \rangle e_{2} - \frac{1}{2} |\alpha|^{2} \theta_{2} e_{2} - \frac{1}{2} \begin{bmatrix} \alpha \\ 0 \end{bmatrix} \langle t, \widehat{\theta} \rangle + \mathcal{O}(|\alpha|^{3}).$$

Now we use that (up to higher order terms) $|\alpha|^2 = |t|^2$ and $\langle t, \hat{\theta} \rangle = \theta_2 \langle t, \pi(\theta) \rangle = -\frac{1}{2}\theta_2 |t|^2$ to see that the first two terms of the above vanish. Hence, the error is equal to than

$$\frac{1}{2}|\langle t, \widehat{\theta} \rangle| + \mathcal{O}(|\alpha|^3) = \frac{1}{4}\theta_2|t|^2 + \mathcal{O}(|\alpha|^3),$$

which was the claim. \Box

Note that due to geometric properties of π , the equation $2\langle \pi(\theta), t \rangle + |t|^2 = 0$ defines a great circle. The proposition thus shows that near the equator on this great circle $\theta_2 \approx 0$, the error is very small. Note that this claim is only of academic interest for us, since points near the equator correspond to points very far away from the principal point, i.e. points that most often will not be captured on an image. We still chose to include it for completeness.

E Proofs

Here, we present the detailed proofs that were left out of the main text.

E.1 Proposition 2.6

Proof of Proposition 2.6. Let $H \in \mathbb{R}^{3,3}$ be the representation of τ in homogeneous coordinates, as in Remark 2.5. We are concerned with the solutions of the equation $\tau(\pi(x)) = \pi(\rho(x))$. The latter is exactly the case when for some $\lambda \in \mathbb{R}$,

$$\lambda Hx = \rho(x) = Rx + v \Leftrightarrow (\lambda H - R)x = v. \tag{8}$$

where R and v are defined through $\rho(x) = Rx + v$. Equation (8) has a unique solution as long as $\lambda H - R$ is invertible. The λ for which this is not the case are the real eigenvalues of $H^{-1}R$. Since $H^{-1}R$ is a real (3 × 3) matrix, it always has at least one eigenvalue, say λ_0 . Since $H^{-1}R$ is not the identity, an eigenvalue λ cannot have (geometric) multiplicity three. As for the case of multiplicity 2, we have the following:

<u>Claim</u>: If there exists a λ such that $M_{\lambda} = \lambda H - R$ has rank 1, $\ker(M_{\lambda}) = \operatorname{span}(e_0, e_1)$.

Proof. If R is the identity, the claim follows immediately from the spectral theory for H. So assume that R is not the identity. R must then have a 2-dimensional invariant subspace W. Let $V = \ker M_{\lambda}$ be the at least two-dimensional kernel V. Since both the spaces are two-dimensional, $V \cap W$ is non-trivial and both R and M_{λ} -invariant. This leaves us with two cases.

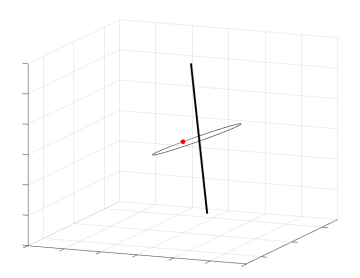
Case 1: R acts as minus the identity on W. Then, we have proven the existence of a $v \in \mathbb{R}^3$ with $M_{\lambda}v = 0$ and Rv = -v. This has the consequence that $\lambda Hv = Rv = -v$, so that v is an eigenvector of H, and thus, in $\operatorname{span}(e_0, e_1)$. Furthermore, $\lambda = -1$. This implies that for the other vector $w \in \ker M_{\lambda}$, $|w| = |Rw| = |\lambda Hv| = |Hw|$, which, by a direct computation, proves that also that vector w is in $\operatorname{span}(e_0, e_1)$. Hence, $V = W = \operatorname{span}(e_0, e_1)$, which was to be proven.

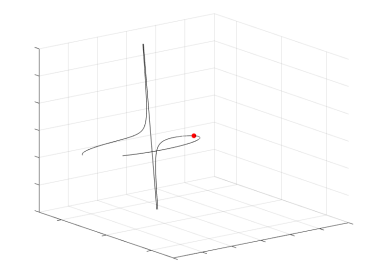
Case 2: W is irreducible. In this case, we must conclude that V = W – otherwise, $W \cap V$ would be an R-invariant one-dimensional subspace of W. In other words, $\lambda H v = R v$ for all $v \in W$. This in particular implies that $\lambda \neq 0$. Now let v_0, v_1, v_2 of \mathbb{R}^3 be an orthonormal basis of \mathbb{R}^3 so that $Rv_0 = v_0$, and consequently $\mathrm{span}(v_1, v_2) = V$. We have

$$\lambda \langle v_i, H^T v_0 \rangle = \lambda \langle H v_i, v_0 \rangle = \langle R v_i, v_0 \rangle = \langle v_i, R^T v_0 \rangle = 0, \quad i = 1, 2.$$

Hence, H^Tv_0 is orthogonal to both v_1 and v_2 , and hence, a multiple of v_0 . v_0 is thus an eigenvector of H^T . Since t is non-zero, at least one if its components are, WLOG $t_0 \neq 0$. Then, v_0 being an eigenvector of H^T implies that $v_0 \in \text{span}(e_1, e_2)$, say $v_0 = \cos(\vartheta)e_2 + \sin(\vartheta)e_1$. Now, since W is the orthogonal complement of v_0 , e_0 must then be in V = W. This has the consequence

$$1 = |e_0|^2 = |Re_0|^2 = |\lambda He_0|^2 = |\lambda|^2.$$
(9)





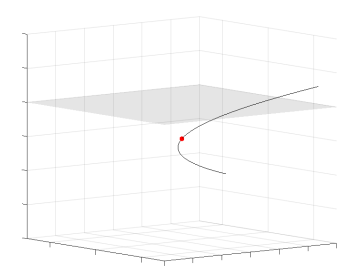


Figure 11: Three possible appearances of the S-set. The dot indicates the camera position.

However, since also $u = -\sin(\theta)e_2 + \cos(\theta)e_1$ is orthogonal to v_0 and thus a member of W = V, we obtain

$$1 = |u|^2 = |Ru|^2 = |\lambda H u|^2 = |\lambda|^2 (1 + \sin(\vartheta)^2 |t|^2).$$
(10)

Equations (9) and (10) can only be true simultaneously if $\sin(\vartheta) = 0$, i.e. that θ is a multiple of π , and $v_0 = e_2$. V = W is as the orthogonal complement of v_0 then equal to $\operatorname{span}(e_0, e_1)$, and the claim has been proven. (\square) The above leaves us with three cases concerning the solveability of (8):

- 1. $\lambda H R$ is regular. Then, the equation has the unique solution $(\lambda H R)^{-1}v$.
- 2. $\lambda H R$ has rank 2. If v lies in the range of $\lambda H R$. Then, the solutions of (8) form a one-dimensional subspace of \mathbb{R}^3 . If not, the equation has no solutions.
- 3. $\lambda H R$ has rank 1. Then, the kernel of $\lambda H R$ is equal to (e_0, e_1) . If v is in the range of $(\lambda H R)$, the set of solution is then a plane parallel to $\operatorname{span}(e_0, e_1)$. Otherwise, the solution-set is empty. In this case, R must further be the identity or $\operatorname{diag}(-1, -1, 1)$

The λ for which cases 2 and 3 occur are exactly the eigenvalues M of $H^{-1}R$. We conclude that S is given by the union of the curve

$$\gamma: \mathbb{R}\backslash M \to \mathbb{R}^3, \quad \lambda \mapsto (\lambda H - R)^{-1}v$$

and possibly sets of the form $w_0 + \ker(\lambda H - R)$ for $\lambda \in M$. The structures of these sets are described by cases 2 and 3 above, and exactly corresponds to the structure claimed in the proposition. The proof is finished.

An illustration of three possible S-sets can be seen in Figure 11

E.2 Proposition 3.1

Proof of Proposition 3.1. 1. Let h_i , i = 0, 1, be homographies with $h_i \circ \pi = \pi \circ R_i$. Then we have for $x \in \mathbb{R}^3$ arbitrary

$$(h_0 \circ h_1)(\pi(x)) = h_0 \circ (h_1 \circ \pi)(x) = (h_0 \circ \pi)(R_1 x) = \pi(R_0 R_1).$$

This proves $h_0 \circ h_1 \in RH$, and also that composition of the homographies is the same as multiplying the representing matrices. This proves that RH is a subgroup of the diffeorphisms, and the map from a homography h to its representing matrix R is an isomorphism between groups.

2. Let $h \in RH$ with associate rotation $R \in SO(3)$ be arbitrary. We need to prove that $\Phi(g \circ h) = (\phi g) \circ h$. Let us first note that $(g \circ h) \circ \pi = (g \circ \pi) \circ R$. Applying the SO(3)-equivariant network Ψ to that relation yields

$$\Psi((g \circ h) \circ \pi) = \Psi((g \circ \pi) \circ R) = \Psi((g \circ \pi)) \circ R.$$

We have $\Psi((g \circ \pi)) = \Phi(g) \circ \pi$. The above, together with $h = \pi \circ R$, hence implies

$$\Phi(q \circ h) \circ \pi = \Phi(q) \circ \pi \circ h = \Phi(q) \circ h \circ \pi,$$

which yields the claim.

E.3 Proposition 3.2

Proof of Prop. 3.2. If G is a subgroup containing pitches and yaws, it must contain all matrices of the form

$$R = R_{x_0}(\alpha)R_{x_1}(\beta)R_{x_0}(\gamma),$$

where $R_{x_0}(\alpha)$ and $R_{x_0}(\gamma)$ are rotations about the x_0 -axis (i.e. pitches) and $R_{x_1}(\beta)$ a rotation about the x_1 -axis (i.e. a yaw). A classical result of differential geometry (the existence of *Euler angles*) however states that each rotation R can be written in that form. Hence, such a subgroup cannot be proper.

E.4 Transforming images on \mathbb{P}^2 to images on PY.

Let us derive a recalculation formula between points $x \in \mathbb{P}^2$, $\alpha \in PY$ and $\theta \in \mathbb{S}^2$. The result is easiest to formulate in polar coordinates in PY and \mathbb{P}^2 .

Proposition E.1. Let $\phi_{\mathbb{S}^2}$ and ϕ_{pol} be the standard spherical and polar coordinate maps, i.e.

$$\phi_{\mathbb{S}^2}(\vartheta,\varphi) = \left[\sin(\vartheta)\cos(\varphi),\sin(\vartheta)\sin(\varphi),\cos(\vartheta)\right]^T, \quad \phi_{\mathrm{pol}}(r,\varphi) = r\left[\cos(\varphi),\sin(\varphi)\right]^T.$$

1. Projection from PY to \mathbb{S}^2 . For $r < \pi$, we have

$$\Phi(\phi_{\text{pol}}(r,\varphi)) = \left(0, \phi_{\mathbb{S}^2}(r,\varphi - \frac{\pi}{2})\right).$$

2. Projection from PY to \mathbb{P}^2 . For $r < \pi/2$, we have

$$\pi(\Phi(\phi_{\text{pol}}(r,\varphi))) = \phi_{\text{pol}}(\tan(r), \varphi - \frac{\pi}{2}).$$

Proof. 1. Let us denote $\alpha = \phi_{\text{pol}}(r, \varphi)$ The curve γ used to define Φ is by Lemma C.2 a geodesic with speed $|\alpha|$. As such, it does not cross $\{\pm e_2\}$ as long as $|\alpha| < \pi$. Since we assumed this, we thus have $\Phi(\alpha) = (0, \gamma(1))$. In order to compute the spherical coordinates of $\gamma(1)$, we again invoke Lemma C.2 to see that $\gamma'(0) = \alpha e_2$. Therefore, γ is the great circle defined by intersecting \mathbb{S}^2 with span $(\alpha e_2, e_2)$. All points in this plane have the same polar angles as $\alpha e_2 = [\alpha_1, -\alpha_0, 0]$, i.e the polar angle of α minus $\frac{\pi}{2}$. Since $\gamma(1)$ is by at a geodesic distance from e_2 of $|\alpha|$, and that this is equal to the azimuth angle, the proof is finished.

2. This is now a trivial consequence of the definition of π

$$\pi(\Phi(\phi_{\mathrm{pol}}(r,\varphi)) = \pi(\phi_{\mathbb{S}^2}(r,\varphi-\tfrac{\pi}{2})) = \tfrac{1}{\cos(r)} \begin{bmatrix} \sin(r)\cos(\varphi,\tfrac{\pi}{2}) \\ \sin(r)\sin(\varphi-\tfrac{\pi}{2}) \end{bmatrix} = \phi_{\mathrm{pol}}(\tan(r),\varphi-\tfrac{\pi}{2}).$$

F Further results

In this section, we report some experimental results not provided in the main article.

F.1 EfficientPose

F.1.1 Choice of depth / rotation representation in the PY setting

In Table 6, we present empirical evidence for the adequacy of our modified depth and rotation representation in the PY setting, as discussed in Section B.1.1. In addition to the ADD(-s)-0.1D metric, we also report average rotation and translation errors, in order to decouple position and orientation when analyzing the performance. These experiments were run a single time rather than the three reruns of the final experiments.

Regarding the frame of reference for the rotation target, we note that in the original \mathbb{P}^2 setting it is best left unaltered, as can be observed from the performance drop of Experiment 2 compared to Experiment 1. Similarly, one can observe significantly lower rotation error for Experiment 4, as compared to Experiment 5. While in this case, the ADD(-s)-0.1D score does however point in the opposite direction, the scores are still comparable. Also note that ADD(-s)-0.1D is not very sensitive to orientation. We conclude that our proposed adjustments to the rotation targets do improve orientation estimation performance, and find them justified.

For the depth representation, comparing Experiment 6 with Experiment 4, there is an obvious performance drop, supporting our adjustments for the PY case. The results when incorporating the same adjustments in the

original \mathbb{P}^2 case are however a bit less conclusive. Since Experiment 6 comes with a performance drop in not only the evaluation metric ADD(-s)-0.1D, but also in the translation error, the proposed depth target does indeed seem more reasonable to predict. However, there is also a reduction in rotation error, and we are unsure of the reason for this. Nevertheless, there is a clear drop in the evaluation metric and we do not find it justified, nor fair, to incorporate the same adjustments for our baseline experiments, and instead leave the rotation as well as depth target representations identical to [10]. We also do not find the depth target adjustment motivated for the \mathbb{P}^2 case.

Image domain	Exp. №	Rot. target frame of reference: x_2 aligned with	Depth target	ADD(-s)- 0.1D	Avg rot error	Avg transl error
	1	optical axis	t_2	79.11%	12.96°	10.67 mm
\mathbb{P}^2	2	per-pixel viewing ray	t_2	78.57%	13.61°	10.83 mm
II.	3	optical axis	cam-to-object distance	78.08%	12.60°	11.10 mm
	4	per-pixel viewing ray	cam-to-object distance	80.54%	12.52°	10.19 mm
PY	5	optical axis	cam-to-object distance	80.88%	13.10°	10.21 mm
	6	per-pixel viewing ray	t_2	79.13%	13.17°	10.79 mm

Table 6: Comparison of different representations for the rotation and depth targets, as discussed in Section B.1.1. For the rotation target, the frame of reference can either be the camera coordinate system (x_2 aligned with optical axis) or the pixel-dependent frame of reference outlined in Section B.1.1 (x_2 aligned with the viewing ray of each pixel). The depth target can either be the final component t_2 of the translation vector, or the camera-to-object distance, also explained in Section B.1.1. Green cells correspond to our proposed target representations, in the \mathbb{P}^2 and PY image domains, respectively, while red cells denote representations we discourage. In addition to the ADD(-s)-0.1D metric, we also report average rotation and translation errors.

F.1.2 Per-object 6D pose estimation results

Table 7 shows the per-object results on Occlusion LINEMOD, and Table 8 shows the per-object results on LINEMOD, in both cases training on the full training set.

Figures 12 and 13 show the per-object results for the limited data study on Occlusion LINEMOD and LINEMOD respectively.

Object		$\phi =$	0		$\phi = 3$			
Object	Original	Baseline	PY	RH _{aug}	Original	Baseline	PY	$\mathrm{RH}_{\mathrm{aug}}$
ape	56.57%	51.21%	52.42%	64.65%	59.39%	55.25%	54.85%	65.15%
can	91.12%	91.32%	92.39%	95.71%	93.27%	94.44%	93.66%	96.68%
cat	68.58%	59.46%	80.87%	68.09%	79.78%	78.99%	84.34%	70.17%
driller	95.64%	95.25%	95.73%	97.77%	97.77%	97.67%	96.90%	98.55%
duck	65.31%	60.73%	64.79%	74.06%	72.71%	65.10%	69.27%	76.56%
eggbox	93.46%	92.96%	94.97%	94.37%	96.18%	95.47%	96.18%	95.47%
glue	85.15%	87.25%	87.65%	89.62%	90.80%	90.01%	89.49%	91.59%
holepuncher	76.53%	78.90%	75.74%	84.71%	81.95%	81.07%	78.01%	85.21 %
Average	79.04%	77.44%	80.47%	83.58%	83.98%	81.94%	82.91%	84.92 %

Table 7: Detailed per-object 6D object pose results according to the ADD(-s)-0.1D metric, with EfficientPose on Occlusion LINEMOD, and train/test split as in [10]. Results are the median over three reruns. The "Baseline" models are retrained and evaluated by us, after some minor modifications, while "Original" refers to the results reported by [10]. Model size is controlled by the ϕ parameter.

F.2 Visual localization on 7-Scenes with DSAC* Tiny

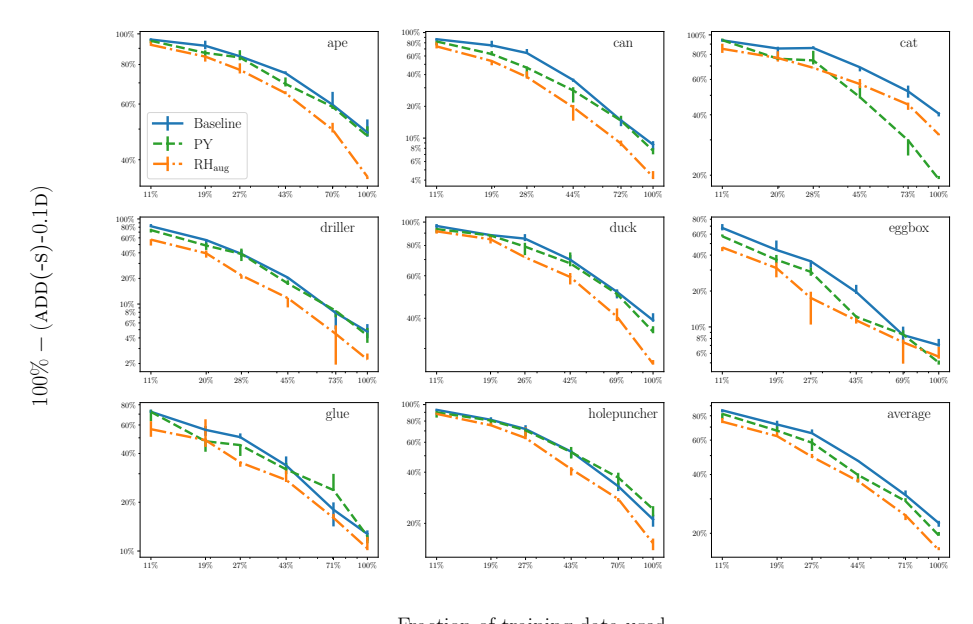
Full per-scene results of the visual localization experiments on 7-Scenes are presented in Table 9. We note that the PY+GeomAug experiment is not only best on average, but also for most scenes.

		Original			
Object	Original	$(\phi = 3)$	Baseline	PY	$\mathrm{RH}_{\mathrm{aug}}$
ape	87.71%	89.43%	80.57%	85.43%	88.48%
benchvise	99.71%	99.71%	99.52%	99.90%	99.90%
cam	97.94%	98.53%	95.20%	97.94%	96.76%
can	98.52%	99.70%	98.23%	98.82%	99.41%
cat	98.00%	96.21%	95.11%	98.10%	98.90%
driller	99.90%	99.50%	99.41%	99.60%	99.60%
duck	90.99%	89.20%	84.13%	89.30%	87.70%
eggbox	100.00%	100.00%	100.00%	99.91%	100.00%
glue	100.00%	100.00%	99.90%	99.90%	100.00%
holepuncher	95.15%	95.72%	93.34%	97.05%	95.53%
iron	99.69%	99.08%	98.88%	99.49%	100.00%
lamp	100.00%	100.00%	99.71%	99.90%	100.00%
phone	97.98%	98.46%	97.41%	98.27%	98.17%
Average	97.35%	97.35%	95.56%	97.09%	97.21%

Table 8: Detailed per-object 6D object pose results according to the ADD(-s)-0.1D metric, with EfficientPose on LINEMOD. Results are the median over three reruns. The "Baseline" model is retrained and evaluated by us, after some minor modifications, while "Original" refers to the results reported by [10]. All models are of type $\phi = 0$, except the second result column which we include for reference.

Scene, Metri	Experiment c	PY+GeomAug	Baseline+GeomAug	RHaug	Baseline	PY
chess	$5\mathrm{cm}/5^{\circ}$	95.00%	94.80%	93.90%	94.20%	94.50%
	med. err. (cm)	1.916	1.791	1.900	1.910	2.022
	med. err. (°)	0.646	0.632	0.659	0.655	0.685
fire	5cm/5°	89.40%	88.10%	88.40%	73.50%	73.00%
	med. err. (cm)	2.114	2.231	2.183	2.713	2.694
	med. err. (°)	0.945	0.952	0.936	1.035	1.031
heads	5cm/5°	94.20%	93.50%	94.40%	84.40%	82.60%
	med. err. (cm)	1.189	1.266	1.260	1.941	1.866
	med. err. (°)	0.867	0.876	0.894	1.256	1.264
office	5cm/5°	77.50%	71.50%	65.90%	74.10%	73.70%
	med. err. (cm)	3.179	3.469	3.842	3.246	3.393
	med. err. (°)	0.924	1.042	1.134	0.894	0.890
pumpkin	5cm/5°	58.50%	58.50%	56.50%	57.60%	61.10%
	med. err. (cm)	4.242	4.186	4.292	4.136	4.056
	med. err. (°)	1.099	1.112	1.106	1.094	1.138
redkitchen	$5\mathrm{cm}/5^{\circ}$	58.80%	56.50%	57.10%	55.50%	53.60%
	med. err. (cm)	4.412	4.526	4.519	4.571	4.718
	med. err. (°)	1.468	1.511	1.549	1.361	1.379
stairs	5cm/5°	33.50%	36.70%	34.50%	4.20%	1.60%
	med. err. (cm)	7.080	6.468	6.926	27.317	32.446
	med. err. (°)	1.372	1.496	1.544	3.622	4.485
Total	5cm/5°	71.60%	69.50%	68.00%	65.50%	64.90%

Table 9: Detailed per-scene results of the experiments with DSAC* Tiny on 7-Scenes. $5 \text{cm}/5^{\circ}$ is the percentage of test examples where the predicted pose is within 5 cm and 5° from the ground truth. The other reported metrics are the median error over the test set in cm and degrees. The *Total* row refers to the percentage of accurate test examples over all scenes.



Fraction of training data used

Figure 12: Detailed per-object results for the limited data experiments per object on Occlusion LINEMOD.

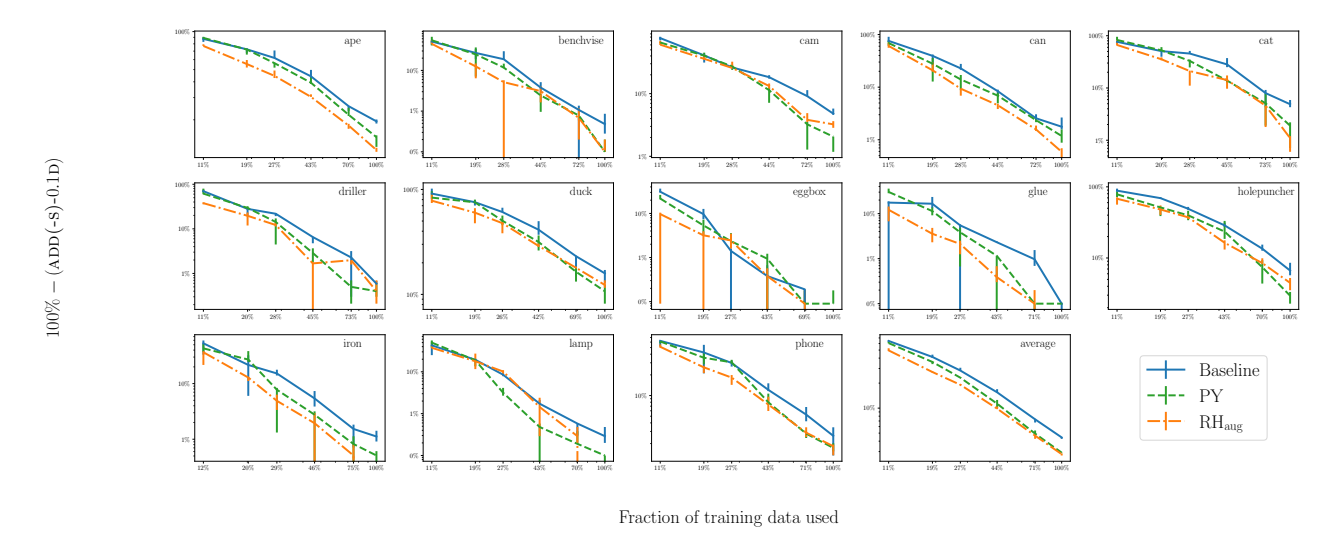


Figure 13: Detailed per-object results for the limited data experiments per object on LINEMOD. Note that some runs scored 100% which is why some error bars drop away outside the plots.